

indiSplit: Bringing Severity Cognizance to Image Decomposition in Fluorescence Microscopy

Ashesh Ashesh
Human Technopole
ashesh.ashesh@fht.org

Florian Jug
Human Technopole
florian.jug@fht.org

Abstract

Fluorescence microscopy, while being a key driver for progress in the life sciences, is also subject to technical limitations. To overcome them, computational multiplexing techniques have recently been proposed, which allow multiple cellular structures to be captured in a single image and later be unmixed. Existing image decomposition methods are trained on a set of superimposed input images and the respective unmixed target images. It is critical to note that the relative strength (mixing ratio) of the superimposed images for a given input is a priori unknown. However, existing methods are trained on a fixed intensity ratio of superimposed inputs, making them not cognizant to the range of relative intensities that can occur in fluorescence microscopy. In this work, we propose a novel method called *indiSplit* that is cognizant of the severity of the above mentioned mixing ratio. Our idea is based on InDI, a popular iterative method for image restoration, and an ideal starting point to embrace the unknown mixing ratio in any given input. We introduce (i) a suitably trained regressor network that predicts the degradation level (mixing asymmetry) of a given input image and (ii) a degradation-specific normalization module, enabling degradation-aware inference across all mixing ratios. We show that this method solves two relevant tasks in fluorescence microscopy, namely image splitting and bleedthrough removal and empirically demonstrate the applicability of *indiSplit* on 5 public datasets. We will release all sources under a permissive license.

1. Introduction

Fluorescence microscopy is a widely utilized imaging technique in the life sciences, enabling researchers to visualize specific cellular and sub-cellular structures with high specificity. It employs distinct fluorescent markers to target different components, which are subsequently captured in separate image channels. The global fluorescence microscopy

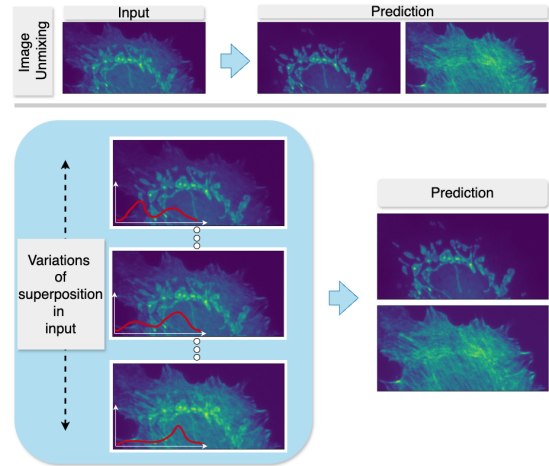


Figure 1. **Handling varying levels of superposition.** For the objective of image unmixing task, superimposed images acquired with Fluorescence microscopy can have varying levels of mixing of the constituent structures. Additionally, insufficiently precise optical filtering often leads to ‘bleedthrough’ wherein a structure of interest gets superimposed with a shadowed presence of another structure. *indiSplit* uniquely addresses these varying levels of structural mixing in the superimposed input images. Unlike existing unmixing methods, *indiSplit*’s architecture adapts to different degrees of superposition and accounts for the resulting variations in pixel intensity distributions (inset plot in red), enabling effective input image normalization and leading to efficient unmixing across diverse mixing ratios.

market, valued at 9.83\$ billion in 2023, is projected to expand significantly in the coming years, reflecting its critical role in advancing biological research [1].

Still, there are practical limitations on the maximum number of structures that can be imaged in one sample. To mitigate this, the idea of imaging multiple structures into a single image channel has recently been gaining popularity [3, 4]. In such approaches, the image produced by the microscope is a superposition of multiple structures and a deep-learning based setup is then used to perform the image

decomposition task, thereby yielding the constituent structures present in the superimposed input as separate images.

While these approaches have been beneficial, they have not explicitly addressed a particular aspect of this problem. The relative intensity of the superimposed structures in the input can vary significantly depending on sample properties, labeling densities, and microscope configuration. For instance, in a superimposed image of nuclei and mitochondria, nuclei may be dominant in their intensities, with the mitochondria showing as relatively faint structures. Existing methods, which are not cognizant to such variations in superposition severity, exhibit performance degradation when applied to images with superposition characteristics different from those encountered during training. We highlight the significance of this issue of severity cognizance by noting that a related problem, known as Bleedthrough, exists in fluorescence microscopy. When imaging a biological structure into a dedicated channel, other structures can become visible due to insufficiently precise optical filtering. In such cases, we say that this other structure “bleeds through” into the currently imaged channel. Note, only if the challenge of relative intensity variation is effectively addressed will a single network ever be able to effectively solve both the image unmixing task and the bleedthrough removal task.

To address this, we propose a novel framework called *indiSplit*, which incorporates the desired cognizance about the superposition severity directly into the inductive bias of the method itself (see Figure 1). For a given superimposed input containing superimposed structures A and B, *indiSplit* explicitly predicts a mixing ratio $t \in [0, 1]$, which quantifies the severity of the superposition, with $t = 0$ meaning that only A is visible, while $t = 1$ conversely meaning that only structure B can be seen. To ensure that the network remains in-distribution for superimposed images with varying superposition severities, we introduce a Severity Cognizant Input Normalization module. This module not only addresses the normalization requirements but also simplifies the inference process, as we show in Section 3. Additionally, leveraging domain-specific knowledge from fluorescence microscopy, we incorporate an aggregation module that enhances the accuracy of the mixing ratio estimation during inference. By integrating these advancements into *indiSplit*, we introduce a method designed to simultaneously address two critical tasks in fluorescence microscopy—image unmixing and bleedthrough removal—by being cognizant of the severity of the superposition.

2. Related Work

In the field of fluorescence microscopy, image decomposition techniques have recently gained significant attention for addressing the image unmixing problem. Seo et al. [26] introduced a linear unmixing approach to separate

k structures, which, however, necessitates k input channels, each representing a distinct superposition of the k structures. More recently, deep learning-based frameworks have emerged [3, 4, 6], capable of predicting individual structures from a single image channel. Ashesh et al. [3] proposed a GPU-efficient meta-architecture, *μSplit*, which leverages contextual information from surrounding regions of the input patch. HVAE [18, 23, 27] and U-Net [24] were used as the underlying architecture for *μSplit*. Three variants of *μSplit* were developed, each optimizing a trade-off between GPU utilization and performance. Further advancements were made with *denoiSplit* [2], which combines unsupervised denoising with supervised image unmixing. More recently *MicroSplit* [6] combined the GPU efficiency of *μSplit* with unsupervised denoising, sampling and calibration of *denoiSplit*. It also provided several image unmixing datasets containing real microscopy images of different structure types. However, existing single-channel input methods [2, 3] typically assume the input to be an average of the two structures, thereby overlooking the variability in superposition intensity present in real-world microscopy images. While the *MicroSplit* analysis successfully quantified the effects of superposition variability, it did not extend to proposing a resolution. This limitation present in existing works highlights the need for more robust approaches to handle the complexities of real imaging data.

Next, we situate the image unmixing task within the broader context of Computer Vision. Image unmixing can be viewed as a specialized form of image translation, where the objective is to map an image from a source data distribution to a corresponding image in a target data distribution. Over the past decade, the field of image translation has witnessed significant advancements, with a wide array of methodologies being proposed. These include architectures such as U-Net [24], generative adversarial networks (GANs) [10, 16, 31], and iterative inference models like diffusion models [20, 25] and flow matching techniques [19, 21, 32], among others. These approaches have demonstrated remarkable capabilities in addressing various challenges in image-to-image transformation tasks, providing a rich foundation for advancing image unmixing techniques.

Iterative models offer the advantage of providing access to intermediate predictions during the inference process. In many such methods, these intermediate predictions—after accounting for noise—closely resemble a superposition of the source and target data distributions. Consequently, when the degradation process itself involves superposition, as is the case in our task, iterative models emerge as a natural choice for modeling the degradation. Literature suggests that the superposition of structures in fluorescence microscopy can be approximated as a linear superposi-

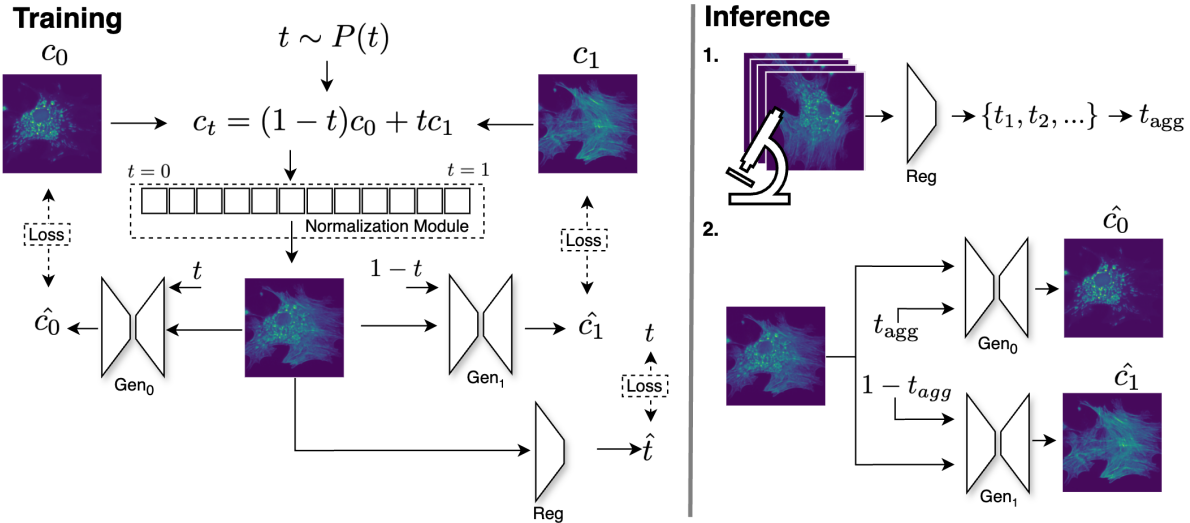


Figure 2. **Schematic overview of the indiSplit framework for handling image superposition at varying severity levels.** (Left) Training pipeline: The input to the system is a superimposed image, generated as a weighted average of two images using a mixing ratio $t \in [0, 1]$. The superimposed image is passed through a normalization module, which performs ratio-specific normalization to ensure zero mean and unit standard deviation. The normalized image is then processed by two generative networks, Gen_0 and Gen_1 , to estimate the individual structures. A regressor network, Reg , is trained to predict the mixing ratio t from a normalized superimposed image. (Right) Inference pipeline: During inference, the mixing ratio t is estimated for a set of superimposed input images using Reg , and the estimates are aggregated to obtain t_{agg} . The normalized superimposed images, along with t_{agg} , are fed into the generative networks Gen_i to recover the individual structures. Thanks to the mixing-ratio specific normalization during training, the normalization during inference is simple and is performed using the mean and standard deviation computed from the set of test input images.

tion [9, 14, 28]. This insight led us to adopt InDI [12], a well-established iterative image restoration method that explicitly models degradation as a linear mixing process. In InDI, the idea is to take the weighted average between the clean target and the degraded input using a scalar mixing ratio to generate a ‘less’ degraded input. The generated input, along with the mixing ratio, are then fed to a network as inputs, and the network is trained to predict the clean target. The inductive bias of this training framework aligns precisely with the linear superposition observed in fluorescence microscopy, making InDI a suitable foundation for our proposed approach.

Finally, we observe that within the broader domain of image translation, the task of image unmixing shares similarities with tasks such as reflection removal, dehazing, and deraining [7, 8, 11, 13]. However, these tasks differ fundamentally from the 2-channel image unmixing problem in fluorescence microscopy in several key aspects like the linearity of the superposition, availability of ground truth for individual channels *etc.*

3. Our Method

Here, we begin by establishing the necessary formal notation. Then, we address the limitations of existing normalization schemes when performing inference from interme-

diated timesteps, and present our improved normalization approach. Finally, we outline the training process, including the loss formulations for the coupled generative networks (Gen_0 and Gen_1) and the regressor network (Reg), as illustrated in Figure 2.

3.1. Problem Definition

Let us denote a set of k image pairs by $C = \{(c_0^1, c_1^1), (c_0^2, c_1^2), \dots, (c_0^k, c_1^k)\}$. We denote by $C_0 = \{c_0^1, c_0^2, \dots\}$ and $C_1 = \{c_1^1, c_1^2, \dots\}$ the two sets of images from the two distributions of images we intend to learn to unmix. For brevity and readability, we will omit the superscript unless needed. For a pair of images ($c_0 \in C_0, c_1 \in C_1$) and a *mixing-ratio* $t \in [0, 1]$, an input to be unmixed is defined by the pixel-wise linear combination

$$c_t = (1 - t)c_0 + tc_1. \quad (1)$$

With this notation at hand, we define the task of *Image Decomposition* as the computational unmixing of a given superimposed image c_t into estimates \hat{c}_0 and \hat{c}_1 . The assessment of the quality of any solution for the image decomposition task is evaluated by computing the similarity between \hat{c}_0 and \hat{c}_1 to the true images c_0 and c_1 , respectively.

3.2. Severity Cognizant Input Normalization

We begin by observing that the normalization procedure for the input patch has not received any special attention in the existing image unmixing works like μ Split [3] and denoSplit [4] and the standard practice of mean and standard deviation based normalization is performed, where the mean and standard deviation computation is done over the entire training data. In InDI [12], where the input also has the same formulation as Eq. 1, c_0 and c_1 are separately normalized according to statistics derived from C_0 and C_1 , respectively. It is important to highlight that a comparable normalization scheme is commonly employed in iterative models that operate with two distinct data distributions, where the objective is to translate from one distribution to another.

To understand why a more involved normalization module is required, let us express for a given mixing ratio t , the mean $\mu(t)$ and the variance $\sigma^2(t)$ of the input c_t . For simplicity of the expression, we assume c_t is a single pixel. Please refer to the supplementary section S.1 for a formulation that holds true for full images. Using Equation 1, one can write

$$\mu(t) = (1 - t)\mathbb{E}[c_0] + t\mathbb{E}[c_1], \quad (2)$$

$$\sigma^2(t) = (1 - t)^2\mathbb{E}[(c_0 - \mathbb{E}[c_0])^2] + t^2\mathbb{E}[(c_1 - \mathbb{E}[c_1])^2] + 2t(1 - t)\text{Cov}[c_0, c_1], \quad (3)$$

where $\text{Cov}[\cdot, \cdot]$ denotes the covariance.

A plausible way to do data normalization would be to standardize the sets of images C_0 and C_1 to have zero mean ($\mathbb{E}[c_0] = \mathbb{E}[c_1] = 0$) and unit variance ($\mathbb{E}[(c_0 - \mathbb{E}[c_0])^2] = \mathbb{E}[(c_1 - \mathbb{E}[c_1])^2] = 1$). In this case, Equations 2 and 3 simplify to $\mu(t) = 0$ and $\sigma^2(t) = t^2 + (1 - t)^2 + 2t(1 - t) \cdot \text{Cov}[c_0, c_1]$, respectively. Note that while $\mu(t)$ is 0 for all t , the variance is a function of t . What this means is that during training, for a given mixing ratio t , the network sees the superimposed images drawn from a distribution of images having zero mean and a standard deviation dependent on t . To get optimal performance during inference, we would want that the images get similarly normalized.

This leads to a subtle but critical complication when we want to do inference on c_t with an arbitrary $t \in [0, 1]$ using a trained indiSplit network. Without knowing the t for a given input, we cannot normalize the input correctly. We support this claim with empirical evidence in Figure S.18.

The solution we propose is to avoid the problem altogether by introducing a *Normalization Module*, ensuring that for every t , $\mu(t) = 0$ and $\sigma^2(t) = 1.0$. To enable this, we must first empirically evaluate what $\mu(t)$ and $\sigma^2(t)$ are for a partition of the interval $[0, 1]$. We chose to split the interval $[0, 1]$ into $n = 100$ equally sized disjoint intervals and compute the mean and variance of n sets of mixed images $C_i = \{c_t : t \in (\frac{i}{n}, \frac{i+1}{n}], i \in [0, \dots, n - 1]\}$, which we compute based on the given image sets C_0 and C_1 . We

store all computed values in a list of tuples D , such that $D[i] = (\mu_i, \sigma_i)$. During training, and after creating a superimposed image c_t as described in Equation 1, we standardize c_t for all $t < 1$ using the mean and variance given in $D[\lfloor tn \rfloor]$.

The normalization module we propose simplifies inference by decoupling input normalization from the mixing ratio. During training, we enforce $\mu(t) = 0$ and $\sigma^2(t) = 1$ across all mixing ratios. During inference, test inputs from a single acquisition can therefore be normalized using the mean and variance computed directly from the images in that acquisition.

3.3. Network Setup

Similar to InDI [12], we use a gaussian noise perturbation on the input. Let c_t^{norm} denote the normalized c_t , with normalization done as described above. Input to the network becomes

$$x_t = c_t^{\text{norm}} + t\epsilon n, \quad (4)$$

with $n \sim \mathcal{N}(0, I)$ and $\epsilon = 0.01$.

Generative network Gen_i . We use two generative networks, Gen_0 and Gen_1 , to give us estimates of c_0^{norm} and c_1^{norm} respectively. As shown in Figure 2, they take as input the normalized superimposed image along with an estimate of the severity of the unmixing to be done. More precisely, unmixed prediction for the channel $i \in \{0, 1\}$ can be expressed as

$$\hat{c}_i^{\text{norm}} = Gen_i(x_t, t\delta_i + (1 - t)\delta_{1-i}), \quad (5)$$

where δ_k denotes the Dirac delta function. Note that the severity of the unmixing to be done for Gen_0 is t and for Gen_1 is $1 - t$.

Time Regressor Network Reg . Our regression network Reg predicts an estimate of t given an input x_t . Crucially, Reg incorporates the same normalization module proposed for the Gen_i networks (Section 3.2), where we demonstrated that normalization statistics for x_t are inherently time-dependent. During inference, inputs must be normalized using statistics consistent with their true t to avoid distributional mismatch. This creates a cyclic dependency: accurate regression of t requires proper normalization, yet normalization itself depends on t , the very quantity being estimated by Reg . Resolving this interdependence is central to our framework’s design.

Next, we utilize domain knowledge to further improve our estimations of t . We know that for all images acquired during a single session at a microscope, the same laser power settings and the same fluorophore types will be used. This means that the mixing-ratio of all these images can be assumed to be the same. Hence we aggregate the t

Dataset		Dominant			Balanced			Weak		
		PSNR	SSIM	LPIPS	PSNR	SSIM	LPIPS	PSNR	SSIM	LPIPS
Hagen et. al	Inp vs Tar	34.1	0.973	0.047	25.1	0.889	0.148	21.2	0.784	0.243
	U-Net	31.8	0.965	0.063	28.2	0.921	0.122	22.0	0.833	0.222
	μ Split _L	33.7	0.965	0.048	31.9	0.961	0.067	23.2	0.857	0.167
	μ Split _R	33.9	0.962	0.046	32.4	0.960	0.062	23.6	0.858	0.165
	μ Split _D	33.1	0.967	0.045	32.4	0.964	0.058	23.4	0.863	0.158
	denoiSplit	32.4	0.958	0.166	31.9	0.954	0.169	23.1	0.851	0.246
	InDI	33.1	0.963	0.043	32.1	0.965	0.052	24.2	0.879	<u>0.138</u>
	indiSplit _{0.5}	34.1	<u>0.979</u>	<u>0.032</u>	<u>33.7</u>	<u>0.975</u>	<u>0.045</u>	25.0	0.881	0.141
	indiSplit _{-agg}	<u>40.6</u>	<u>0.994</u>	<u>0.011</u>	<u>33.3</u>	<u>0.976</u>	<u>0.046</u>	<u>28.0</u>	<u>0.929</u>	<u>0.123</u>
	indiSplit	40.9	0.994	0.011	33.9	0.977	0.046	29.3	0.934	0.123
HTLIF24	Inp vs Tar	42.3	0.989	0.018	33.3	0.946	0.075	29.5	0.881	0.139
	U-Net	45.9	0.980	0.023	44.6	0.986	0.016	36.0	0.939	0.066
	μ Split _L	46.7	0.978	0.024	45.1	0.986	0.016	36.6	0.940	0.068
	μ Split _R	46.4	0.978	0.024	45.1	0.986	0.016	36.5	0.940	0.068
	μ Split _D	45.9	0.979	0.024	44.9	0.986	0.016	36.4	0.942	0.066
	denoiSplit	44.8	0.981	0.029	42.9	0.985	0.025	35.8	0.938	0.075
	InDI	45.2	0.976	0.031	43.9	0.991	0.012	37.6	0.963	0.055
	indiSplit _{0.5}	45.9	0.987	0.015	<u>45.1</u>	0.991	0.013	37.4	0.951	0.065
	indiSplit _{-agg}	<u>50.1</u>	<u>0.997</u>	<u>0.003</u>	<u>44.0</u>	<u>0.993</u>	<u>0.010</u>	<u>38.8</u>	<u>0.975</u>	<u>0.035</u>
	indiSplit	51.8	0.998	0.002	45.5	0.994	0.009	39.9	0.976	0.034
BioSR	Inp vs Tar	33.9	0.937	0.119	24.1	0.746	0.311	21.1	0.504	0.498
	U-Net	37.2	0.924	0.066	33.7	0.958	0.059	25.6	0.740	0.292
	μ Split _L	37.8	0.918	0.066	33.5	0.959	0.051	25.7	0.738	0.291
	μ Split _R	37.8	0.921	0.060	33.0	0.960	0.049	25.7	0.748	0.276
	μ Split _D	37.5	0.915	0.070	32.6	0.956	0.059	25.2	0.744	0.278
	denoiSplit	36.4	0.929	0.083	33.1	0.957	0.086	25.3	0.733	0.322
	InDI	35.9	0.917	0.054	33.4	0.953	0.050	26.3	0.802	0.211
	indiSplit _{0.5}	37.3	0.957	0.033	<u>35.0</u>	<u>0.967</u>	<u>0.037</u>	26.4	0.770	0.236
	indiSplit _{-agg}	<u>39.3</u>	<u>0.986</u>	<u>0.012</u>	33.7	0.965	0.039	<u>27.2</u>	<u>0.868</u>	<u>0.153</u>
	indiSplit	40.1	0.987	0.011	35.3	0.973	0.033	28.7	0.889	0.130
HTT24	Inp vs Tar	38.7	0.978	0.015	29.6	0.900	0.075	25.8	0.783	0.149
	U-Net	37.9	0.963	0.042	37.5	0.965	0.020	30.1	0.883	0.059
	μ Split _L	37.3	0.953	0.046	36.6	0.959	0.021	29.7	0.880	0.059
	μ Split _R	37.6	0.954	0.046	36.9	0.959	0.021	29.9	0.880	0.059
	μ Split _D	37.5	0.954	0.045	36.8	0.960	0.021	29.8	0.880	0.059
	denoiSplit	37.3	0.954	0.055	37.5	0.964	0.028	31.0	0.896	0.062
	InDI	37.6	0.962	0.034	36.5	0.966	0.017	30.5	0.909	0.057
	indiSplit _{0.5}	38.1	0.984	0.018	<u>38.6</u>	<u>0.979</u>	0.008	31.4	0.902	0.063
	indiSplit _{-agg}	<u>43.4</u>	<u>0.993</u>	<u>0.002</u>	38.2	<u>0.979</u>	<u>0.007</u>	<u>33.7</u>	<u>0.939</u>	<u>0.030</u>
	indiSplit	44.5	0.995	0.001	39.1	0.981	0.005	34.7	0.943	0.028
PaviaATN	Inp vs Tar	31.0	0.932	0.104	22.3	0.754	0.294	18.2	0.548	0.480
	U-Net	29.3	0.870	0.210	25.4	0.743	0.346	21.2	0.568	0.500
	μ Split _L	27.0	0.889	0.133	24.3	0.780	0.241	21.1	0.622	0.396
	μ Split _R	27.4	0.905	0.120	24.7	0.800	0.228	21.1	0.639	0.387
	μ Split _D	27.9	0.908	0.127	25.2	0.808	0.241	21.3	0.648	0.399
	denoiSplit	27.3	0.857	0.772	26.2	0.843	0.794	21.8	0.750	0.824
	InDI	29.9	0.943	0.131	23.9	0.858	0.192	21.7	0.741	<u>0.248</u>
	indiSplit _{0.5}	29.0	0.948	0.082	<u>27.1</u>	<u>0.904</u>	<u>0.135</u>	21.2	0.774	0.226
	indiSplit _{-agg}	<u>33.9</u>	<u>0.976</u>	<u>0.035</u>	<u>27.1</u>	0.903	0.166	<u>23.9</u>	<u>0.819</u>	0.387
	indiSplit	35.1	0.977	0.033	27.6	0.907	<u>0.155</u>	24.3	0.823	0.377

Table 1. **Quantitative evaluation of unmixing performance across five tasks.** We categorize the input into three regimes based on the dominance of the target channel: *dominant* ($w \in \{0.9, 0.8, 0.7\}$), *balanced* ($w \in \{0.6, 0.5, 0.4\}$), and *weak* ($w \in \{0.3, 0.2, 0.1\}$). The reported metric values are averaged across both channels and all values of w within each regime. To account for the varying difficulty of the regimes, we include a comparison between the input and the target in the first row for each dataset. Metrics include Multiscale SSIM (MS-SSIM) [29] and range-invariant PSNR [30]. The grayed and underlined entries indicate the best and second-best results for each metric, respectively.

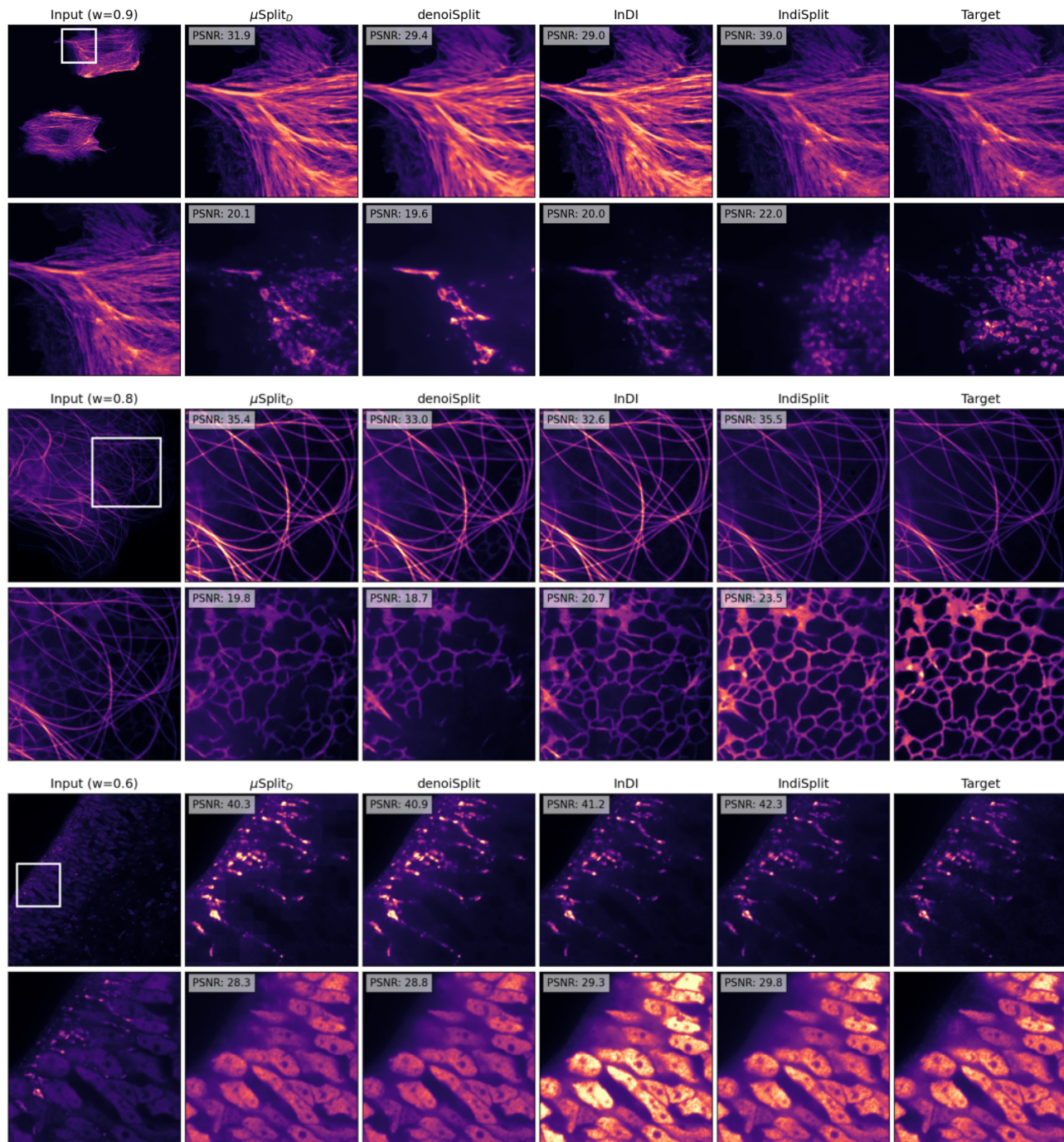


Figure 3. **Qualitative evaluation of unmixing performance.** We show qualitative evaluation on Hagen et al. [15] (top panel), BioSR [17] (middle panel), and HTT24 [6] (bottom panel). For each dataset, the full input frame (top-left) and a zoomed-in input patch (bottom-left) are displayed. Predictions and corresponding targets (last column) are for the inset. They are shown for both channels, with each channel displayed in a separate row. PSNR values are also reported for the inset. The mixing ratio w indicated above the input column corresponds to the first channel, with the second channel naturally having a ratio of $(1 - w)$. Additional qualitative evaluations across different w values for all datasets are provided in the supplementary section S.9.

values estimated from the set of images belonging to a single session and use that during inference. The aggregation

is implemented as a simple arithmetic mean of the t values obtained for individual images in the session. In the supple-

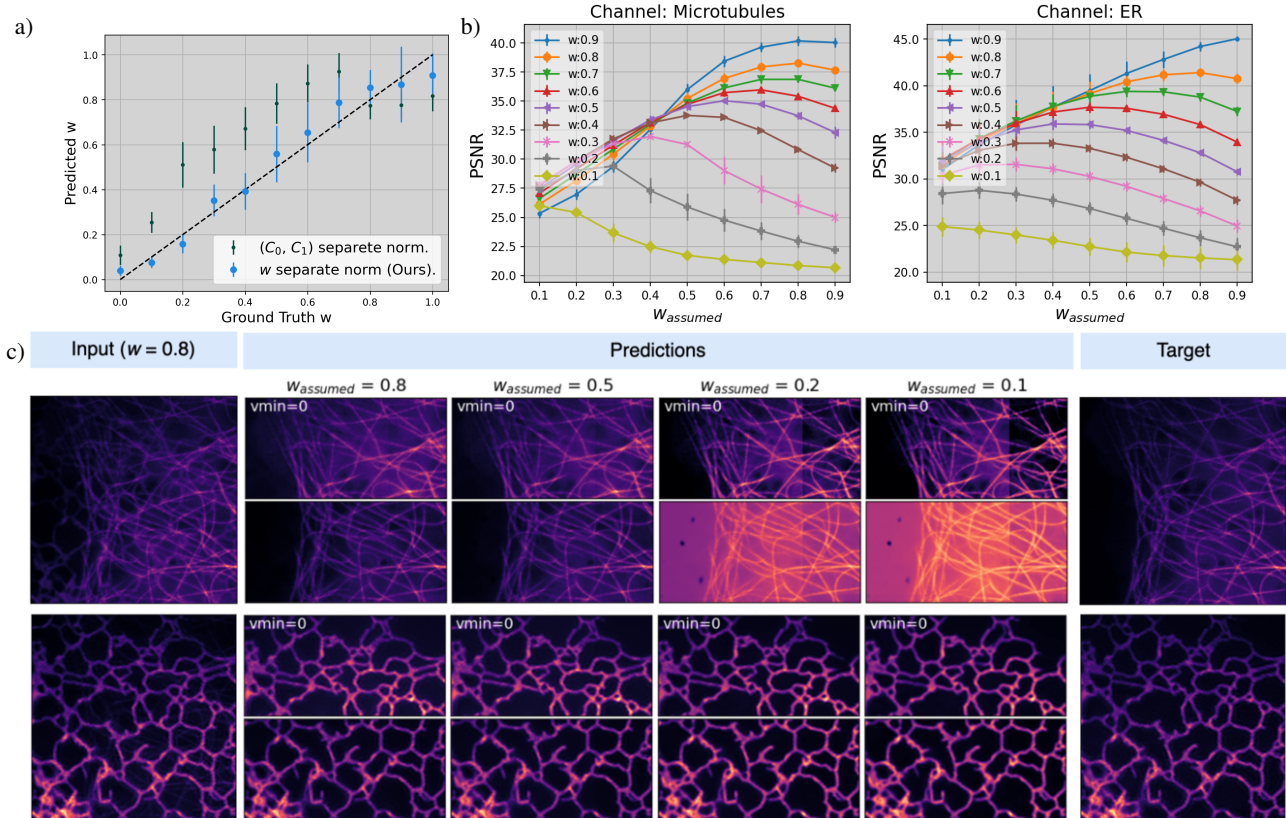


Figure 4. **Performance evaluation of the regressor network Reg .** (a) *Justification for the normalization module on the Hagen et al. dataset:* The conventional normalization of C_0 and C_1 leads to out-of-distribution issues during test evaluation. In contrast, our w -specific normalization scheme demonstrates superior performance. (b) *Quantitative evaluation of performance degradation with incorrect w during inference:* This analysis highlights the sensitivity to inaccurate predictions by Reg . The x-axis represents the assumed w during inference, while the y-axis quantifies the resulting performance degradation. (c) *Qualitative evaluation on the BioSR dataset with varying w during inference:* Predictions are shown for each channel (two rows) under different assumed w values. For each w , the input is divided into upper and lower halves, displayed in two sub-rows. The first sub-row ignores negative pixel values during visualization, while the second sub-row uses default visualization. Observations include tiling artifacts, disappearance of structures, and increased "crispness" of microtubule curves as lower w values are used during inference.

mentary section S.5, we experiment with different aggregation methods.

Distribution for $p(t)$. To model $p(t)$, we modify the distribution denoted as ' $linear_a$ ' in InDI, adapting it to

$$p(t) = \frac{1}{1+a}U[0, 1] + \frac{a}{1+a}\delta_{0.5}, \quad (6)$$

with $a = 1$ in all our experiments. Unlike InDI, where more weight was given via the Dirac delta distribution to $t = 1$, we need more weight on $t = 0.5$. It is so because this is an image unmixing task where the input will contain both structures but c_1 does not contain c_0 at all (and vice versa). We use MAE and MSE loss to train Gen_i and Reg networks, respectively.

4. Results

In all qualitative figures and tables, we define the input as

$$x_w = w * C_{\text{'wanted'}} + (1 - w) * C_{\text{'other'}} \quad (7)$$

This notation allows us to relate w directly to the strength of the channel we are evaluating. The value of w determines the nature of the prediction task. When $w = 0.1$, the objective is to predict the dim structure within the superimposed input. Conversely, when $w = 0.9$, the task shifts to identifying and removing the dim structure, effectively isolating the dominant structure. This latter scenario is commonly referred to as the bleed-through removal task in the field.

Datasets and Unmixing Tasks. We tackle five tasks coming from five real microscopy datasets, namely Hagen et

	HT-LIF24			HT-T24		
	PSNR	SSIM	LPIPS	PSNR	SSIM	LPIPS
Inp vs Tar	32.9	.947	.193	29.4	.894	.152
U-Net	40.7	.990	.021	35.6	.955	.015
μ Split _L	40.6	.990	.022	35.0	.949	.017
μ Split _R	40.9	.991	.021	35.1	.950	.017
μ Split _D	40.9	.991	.021	35.2	.950	.017
denoiSplit	39.8	.988	.032	36.6	.961	.030
InDI	41.2	.992	.012	34.4	.946	.037
indiSplit _{0.5}	41.1	.993	.016	35.9	.956	.017
indiSplit _{-agg}	40.5	.991	.015	35.6	.955	.019
indiSplit	40.9	.992	.015	36.0	.957	.017

Table 2. **Quantitative evaluation on superimposed raw microscopy images.** For the HT-LIF24 and HT-T24 datasets, we have access to the raw superimposed images acquired roughly with ‘Balanced’ channel intensities. We present quantitative evaluation on them in this table. In this table, we denote by ‘SSIM’, the microscopy metric MicroMS3IM [5], a variant of SSIM specifically designed for comparing images with different intensity distributions. The grayed and underlined entries indicate the best and second-best results for each metric, respectively.

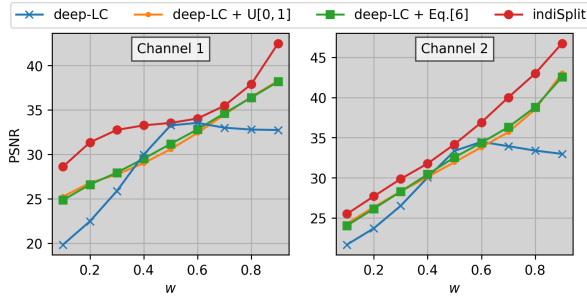


Figure 5. **Analysis of factors contributing to the superior performance of indiSplit.** We investigate one key factor behind indiSplit’s enhanced performance: its exposure to inputs with varying levels of mixing during training. To analyze its effect, we introduce two augmentations to the input generation process of μ Split_D [3], one of our baselines, allowing it to also observe different mixing levels during training. While these augmented μ Split_D variants show improved performance over the vanilla μ Split_D, indiSplit consistently outperforms them across most mixing ratios w . Specifically, we compare indiSplit against the best-performing baseline for each w and each channel, and find that indiSplit achieves an average improvement of 2.4 dB PSNR.

al. [15], BioSR [17], HTT24 [6], HTLIF24 [6] and PaviaATN [3]. From the BioSR dataset, we tackle the ER vs. Microtubules task. From the Hagen et al., we tackle the Actin vs. Mitochondria task. From HTT24, we tackle the SOX2 vs. MAP2 task. From HTLIF24 we choose the Microtubules vs. Centromere task and from PaviaATN the Actin vs. Tubulin task. In addition to individual channels, the HTT24 and HTLIF24 datasets also include superimposed inputs directly captured using a microscope.

If we were to infer the mixing ratio w solely based on the laser power ratios employed for the two structures in these datasets, we would obtain values of $w = 0.5$ and $w = 0.41$ for HTT24 and HTLIF24, respectively. For these two datasets, we additionally evaluate on these superimposed images.

Baselines. As our first baseline, we use a supervised U-NET [24]. We use the implementation provided by [3]. Next, we use the three architectures proposed in μ Split [3], namely Lean-LC, Regular-LC and Deep-LC as baselines which we refer to as μ Split_L, μ Split_R and μ Split_D, respectively. For the Hagen et al. [15] and the PaviaATN [3] data, we used publicly available pretrained models. Next, we use denoiSplit as a baseline with increased patch size (from 128 to 512) to ensure a fair comparison with indiSplit. All other hyperparameters present in the official implementations for denoiSplit were left unchanged. Finally, we use InDI itself as a baseline. Since there is no available official implementation for InDI, we implemented it ourselves. To ensure a fair comparison, we utilized an identical set of hyperparameters for both InDI and indiSplit implementations. Furthermore, for the same reason, these networks were designed to have a comparable parameter count to the μ Split variants and denoiSplit.

For our InDI baseline, we use $t = 0.5$ during inference and use the $p(t)$ defined in Equation 6 during training. Please refer to the supplement for more details on these baselines. To evaluate the models on superimposed images directly captured with a microscope, we trained all models with synthetic inputs and used them for evaluation.

To separately showcase the benefits of the *Reg* network and the aggregation operation, we have two variants of indiSplit namely indiSplit_{0.5} and indiSplit_{-agg} as additional baselines. indiSplit_{0.5} does not use the *Reg* network, and instead always uses $t = 0.5$ during inference. indiSplit_{-agg} uses the *Reg* network, but does not perform aggregation.

Quantitative Evaluation. In Table 1, we present quantitative results. Here, we consider three input regimes, namely ‘Dominant’, ‘Balanced’ and ‘Weak’, each differing from the other on the strength of the structure we are interested in. While in the *Weak* regime, the structure we desire to extract from the input is barely present, the desired structure is dominant in inputs from the ‘Dominant’ regime. Within the lexicon of microscopy, inputs derived from the Strong regime are designated as exhibiting ‘bleedthrough’. For each regime, we average the performance over the two channels and the 3 different w values as mentioned in Table 1. Please refer to the supplementary section S.2 for more details on used evaluation procedures.

From Table 1, it is clear that indiSplit does a good job across all input regimes, and especially for the *Dominant* regime, that is, for higher w values. This result shows that a single trained indiSplit network, which is cognizant of the severity of superposition, can solve both the bleedthrough removal task and image unmixing task. As mentioned above, we also have real superimposed images for the balanced regime in HTT24 and HTLIF24 dataset. We show the quantitative evaluation in Table 2. Although all baseline methods are optimized for the balanced regime, indiSplit achieves competitive performance even under these conditions, as evidenced by the results in Table 1 and Table 2. This can be attributed, in part, to the normalization schemes used in μ Split and denoiSplit, which penalize performance when the normalization statistics for the test images are computed from the test images themselves. For further details, refer to Supplementary Section S.3 and Table S.6.

Utility of the Normalization Module. The utility of the normalization module can be inferred by comparing InDI with our indiSplit_{0.5} variant in Table 1 with our variant outperforming by 1.2db PSNR on average across all regimes and all four datasets. Note that all hyper-parameters for the InDI and Gen_i networks of indiSplit_{0.5} are identical, and the only difference is in the normalization. One can also note its utility by comparing the performance of *Reg* network trained with or without our normalization scheme in Figure 4(a). One can observe the empirical dependence of the standard deviation of patches with and without our normalization scheme in Supplementary Figure S.18.

Utility of Aggregation. Across Tables 1 and 2 indiSplit outperforms the ablated network indiSplit_{-agg} on all tasks for the PSNR metric, thereby clearly justifying the utility of the aggregation operation. In the supplementary section S.5, we experiment with different aggregation methodologies.

Utility of *Reg*. One can observe the utility of using *Reg* when comparing indiSplit_{0.5} with indiSplit_{-agg} with the latter variant outperforming the former across several tasks in Table 1. It is worth noting that the improved performance is more pronounced the more asymmetric an input is (*Dominant* vs. *Weak*). We argue that indiSplit_{0.5}'s assumption of $t = 0.5$ becomes reasonable in the *Balanced* input regime, leading to its competitive performance in this regime.

Degradation Analysis for *Reg*. In Figure 4(b), with BioSR dataset, we analyze the performance degradation when using increasing incorrect estimates for w during inference. We evaluate indiSplit using a fixed w (x-axis) in the inference, while the inputs have been created with a different w (see legend). As expected, the larger the difference

between the assumed w and the actual w , the stronger is the performance degradation. We also show the qualitative effect of using increasingly incorrect w during inference in Figure 4(c).

Exploring Augmentations. One of the critical advantages indiSplit and InDI have over other baselines is that during training, they observe inputs with different mixing ratios and so naturally, it makes it easier for them to outperform them. However, InDI cannot leverage this advantage since it does not have the *Reg* network. To analyze this aspect, we experimented with two different augmentations in the training procedure of μ Split_D, the most powerful variant of μ Split. During training μ Split_D, instead of creating the input by simply summing the two channel images, we instead compute $inp = tc_0 + (1 - t)c_1$, where t is sampled from $p(t)$. We work with two variants of $p(t)$: (i) $p(t) = U[0, 1]$ and (ii) $p(t)$ as defined in Eq. 6. Results shown in Figure 5 demonstrate that these augmentations help μ Split_D to improve performance for w further away from 0.5 along with some performance degradation for $w = 0.5$. However, indiSplit still consistently outperforms the best of all three variants by 2.4db PSNR on average. We note that the suboptimal normalization settings for μ Split_D also contribute to this, which is analyzed in the supplement. In Supplementary Figure S.2, we analyze the effect of normalization across these augmentations.

Application to Tasks on Natural Images. While this work primarily focuses on fluorescence microscopy, we believe our framework can be extended to address image restoration challenges in natural images. However, such tasks often require different inductive biases to achieve optimal performance. For instance, in motion deblurring, the severity of degradation can vary significantly across different regions within a single image. However, as a proof of concept, we demonstrate in the supplementary section S.7 that accounting for the severity of degradation provides tangible benefits for the motion deblurring of natural images.

5. Conclusion and Discussion

In this work, we introduce indiSplit, a network designed to simultaneously address two key challenges in fluorescence microscopy: image unmixing and bleedthrough removal. Our architecture is explicitly designed to account for the severity of the superposition that needs to be unmixed. We also identify limitations in the normalization methodologies of existing image unmixing approaches and propose an alternative normalization strategy that is better suited for inputs with varying levels of superposition. Additionally, we developed an aggregation module that improves the estimation of mixing ratios. Looking ahead, we plan to

extend `indiSplit` to handle noisy microscopy data. The motivation would be to add unsupervised denoising capability to our `indiSplit` network. Additionally, we plan to extend the application of `indiSplit` to other tasks, including image restoration for natural images, as we believe in the potential of our severity cognizant approach.

Acknowledgments

The authors thank Mauricio Delbracio and Peyman Milanfar from Google Research for useful discussions and technical guidance. This work was supported by the European Commission through the Horizon Europe program (IMAGINE project, grant agreement 101094250-IMAGINE) as well as core funding of Fondazione Human Technopole. We want to thank the IT and HPC team at Human Technopole for access to their compute infrastructure and all members of the Jug Group and our image analysis facility NoBIAS for helpful discussions and support.

References

- [1] Fluorescence Microscopy Market Size, Share, Trends And Forecast. [1](#)
- [2] Ashesh and Florian Jug. `denoisplit`: a method for joint image splitting and unsupervised denoising. *ArXiv*, abs/2403.11854, 2024. [2](#)
- [3] Ashesh, Alexander Krull, Moises Di Sante, Francesco Silvio Pasqualini, and Florian Jug. `μSplit`: image decomposition for fluorescence microscopy. 2023. [1](#), [2](#), [4](#), [8](#)
- [4] Ashesh Ashesh and Florian Jug. `denoisplit`: A method for joint microscopy image splitting and unsupervised denoising. In *Computer Vision – ECCV 2024*, pages 222–237, Cham, 2025. Springer Nature Switzerland. [1](#), [2](#), [4](#)
- [5] Ashesh Ashesh, Joran Deschamps, and Florian Jug. `MicroSSIM`: Improved Structural Similarity for Comparing Microscopy Data. In *BIC Workshop, ECCV*, Milan, 2024. [8](#)
- [6] Ashesh Ashesh, Federico Carrara, Igor Zubarev, Vera Galinova, Melisande Croft, Melissa Pezzotti, Daozheng Gong, Francesca Casagrande, Elisa Colombo, Stefania Giusani, Elena Restelli, Eugenia Cammarota, Juan Manuel Battagliotti, Nikolai Klena, Moises Di Sante, Gaia Pigino, Elena Taverna, Oliver Harschnitz, Nicola Maghelli, Norbert Scherer, Damian Edward Dalle Nogare, Joran Deschamps, Francesco Pasqualini, and Florian Jug. `Microsplit`: Semantic unmixing of fluorescent microscopy data. *bioRxiv*, 2025. [2](#), [6](#), [8](#)
- [7] Yuval Bahat and Michal Irani. Blind dehazing using internal patch recurrence. In *2016 IEEE International Conference on Computational Photography (ICCP)*, pages 1–9, 2016. [3](#)
- [8] Dana Berman, Tali Treibitz, and Shai Avidan. Non-local image dehazing. In *2016 IEEE Conference on Computer Vision and Pattern Recognition (CVPR)*, pages 1674–1682. IEEE, 2016. [3](#)
- [9] Kun Chen, Rui Yan, Limin Xiang, and Ke Xu. Excitation spectral microscopy for highly multiplexed fluorescence imaging and quantitative biosensing. *Light: Science & Applications*, 10(1):97, 2021. [3](#)
- [10] Yunje Choi, Minje Choi, Munyoung Kim, Jung-Woo Ha, Sunghun Kim, and Jaegul Choo. Stargan: Unified generative adversarial networks for multi-domain image-to-image translation. In *Proceedings of the IEEE Conference on Computer Vision and Pattern Recognition*, 2018. [2](#)
- [11] Tali Dekel, Michael Rubinstein, Ce Liu, and William T Freeman. On the effectiveness of visible watermarks, 2017. [3](#)
- [12] Mauricio Delbracio and Peyman Milanfar. Inversion by direct iteration: An alternative to denoising diffusion for image restoration. *Transactions on Machine Learning Research*, 2023. Featured Certification. [3](#), [4](#), [S.22](#)
- [13] Yossi Gandelsman, Assaf Shocher, and Michal Irani. “Double-DIP”: Unsupervised image decomposition via coupled deep-image-priors, 2019. Accessed: 2022-2-14. [3](#)
- [14] Mark A. J. Gorris, Altuna Halilovic, Katrin Rabold, Anne van Duffelen, Iresha N. Wickramasinghe, Dagmar Verweij, Inge M. N. Wortel, Johannes C. Textor, I. Jolanda M. de Vries, and Carl G. Figdor. Eight-Color Multiplex Immunohistochemistry for Simultaneous Detection of Multiple Immune Checkpoint Molecules within the Tumor Microenvironment. *Journal of Immunology (Baltimore, Md.: 1950)*, 200(1):347–354, 2018. [3](#)
- [15] Guy M Hagen, Justin Bendesky, Rosa Machado, Tram-Anh Nguyen, Tanmay Kumar, and Jonathan Ventura. Fluorescence microscopy datasets for training deep neural networks. *Gigascience*, 10(5), 2021. [6](#), [8](#)
- [16] Phillip Isola, Jun-Yan Zhu, Tinghui Zhou, and Alexei A Efros. Image-to-image translation with conditional adversarial networks. *CVPR*, 2017. [2](#)
- [17] Luhong Jin, Jingfang Liu, Heng Zhang, Yunqi Zhu, Haixu Yang, Jianhang Wang, Luhao Zhang, Yingke Xu, Cuifang Kuang, and Xu Liu. Deep learning permits imaging of multiple structures with the same fluorophores. *bioRxiv*, 2023. [6](#), [8](#)
- [18] Diederik P Kingma and Max Welling. An introduction to variational autoencoders. 2019. [2](#)
- [19] Nikita Kornilov, Alexander Gasnikov, and Alexander Korotkin. Optimal flow matching: Learning straight trajectories in just one step. *ArXiv*, abs/2403.13117, 2024. [2](#)
- [20] Bo Li, Kaitao Xue, Bin Liu, and Yu-Kun Lai. `Bdbm`: Image-to-image translation with brownian bridge diffusion models. In *Proceedings of the IEEE/CVF Conference on Computer Vision and Pattern Recognition*, pages 1952–1961, 2023. [2](#)
- [21] Yaron Lipman, Ricky T. Q. Chen, Heli Ben-Hamu, Maximilian Nickel, and Matthew Le. Flow matching for generative modeling. *International Conference on Learning Representations*, abs/2210.02747, 2022. [2](#)
- [22] Seungjun Nah, Tae Hyun Kim, and Kyoung Mu Lee. Deep Multi-scale Convolutional Neural Network for Dynamic Scene Deblurring. In *2017 IEEE Conference on Computer Vision and Pattern Recognition (CVPR)*, pages 257–265, Los Alamitos, CA, USA, 2017. IEEE Computer Society. [S.4](#)
- [23] Mangal Prakash, Mauricio Delbracio, Peyman Milanfar, and Florian Jug. Interpretable unsupervised diversity denoising and artefact removal. 2021. [2](#)

- [24] Olaf Ronneberger, Philipp Fischer, and Thomas Brox. U-Net: Convolutional Networks for Biomedical Image Segmentation, 2015. arXiv:1505.04597 [cs]. [2](#), [8](#)
- [25] Chitwan Saharia, William Chan, Huiwen Chang, Chris Lee, Jonathan Ho, Tim Salimans, David Fleet, and Mohammad Norouzi. Palette: Image-to-image diffusion models. In *ACM SIGGRAPH 2022 Conference Proceedings*, New York, NY, USA, 2022. Association for Computing Machinery. [2](#)
- [26] Junyoung Seo, Yeonbo Sim, Jeewon Kim, Hyunwoo Kim, In Cho, Hoyeon Nam, Young-Gyu Yoon, and Jae-Byum Chang. PICASSO allows ultra-multiplexed fluorescence imaging of spatially overlapping proteins without reference spectra measurements. *Nat. Commun.*, 13(1):1–17, 2022. [2](#)
- [27] Casper Kaae Sønderby, Tapani Raiko, Lars Maaløe, Søren Kaae Sønderby, and Ole Winther. Ladder variational autoencoders. In *Proceedings of the 30th International Conference on Neural Information Processing Systems*, page 3745–3753, Red Hook, NY, USA, 2016. Curran Associates Inc. [2](#)
- [28] Alex M. Valm, Sarah Cohen, Wesley R. Legant, Justin Melunis, Uri Hershberg, Eric Wait, Andrew R. Cohen, Michael W. Davidson, Eric Betzig, and Jennifer Lippincott-Schwartz. Applying systems-level spectral imaging and analysis to reveal the organelle interactome. *Nature*, 546(7656):162–167, 2017. [3](#)
- [29] Z. Wang, E.P. Simoncelli, and A.C. Bovik. Multiscale structural similarity for image quality assessment. In *The Thirty-Seventh Asilomar Conference on Signals, Systems and Computers, 2003*, pages 1398–1402 Vol.2, 2003. [5](#)
- [30] Martin Weigert, Uwe Schmidt, Tobias Boothe, Andreas Müller, Alexander Dibrov, Akanksha Jain, Benjamin Wilhelm, Deborah Schmidt, Coleman Broaddus, Siân Culley, Maurício Rocha-Martins, Fabián Segovia-Miranda, Caren Norden, Ricardo Henriques, Marino Zerial, Michele Solimena, Jochen Rink, Pavel Tomancak, Loïc Royer, Florian Jug, and Eugene W Myers. Content-aware image restoration: pushing the limits of fluorescence microscopy. *Nature Publishing Group*, 15(12):1090–1097, 2018. [5](#)
- [31] Jun-Yan Zhu, Taesung Park, Phillip Isola, and Alexei A. Efros. Unpaired image-to-image translation using cycle-consistent adversarial networks. In *2017 IEEE International Conference on Computer Vision (ICCV)*, pages 2242–2251, 2017. [2](#)
- [32] Yixuan Zhu, Wenliang Zhao, Ao Li, Yansong Tang, Jie Zhou, and Jiwen Lu. FlowIE: Efficient Image Enhancement via Rectified Flow . In *2024 IEEE/CVF Conference on Computer Vision and Pattern Recognition (CVPR)*, pages 13–22, Los Alamitos, CA, USA, 2024. IEEE Computer Society. [2](#)

SUPPLEMENTARY MATERIAL

indiSplit: Bringing Severity Cognizance to Image Decomposition in Fluorescence Microscopy

Ashesh Ashesh, Florian Jug
Jug Group, Fondazione Human Technopole, Milano, Italy,

S.1. Severity Cognizant Input Normalization

In this section, we extend the formulations presented in Section 3.2 to accommodate images of arbitrary dimensions $H \times W$. Let $p_t[i, j]$ be a random variable denoting a pixel intensity value present in $c_t \in C_t$ at the location (i, j) . Let us now compute the mean ($\mu(t)$) and variance ($\sigma^2(t)$) of c_t .

$$\mu(t) = \frac{1}{P} \sum_{i,j} p_t[i, j], \quad (1)$$

and

$$\sigma^2(t) = \frac{1}{P} \sum_{i,j} p_t[i, j]^2 - \mu(t)^2, \quad (2)$$

where P is the total number of pixels in c_t . Note that $\mu(t)$ and $\sigma(t)$ are also random variables. Their expected values $\mathbb{E}[\mu(t)]$ and $\mathbb{E}[\sigma(t)]$ are typically used for normalization.

Next, describing $\mu(t)$ in terms of random variables p_0 and p_1 , we get,

$$\begin{aligned} \mu(t) &= \frac{1}{P} \sum_{i,j} ((1-t)p_0[i, j] + tp_1[i, j]) \\ &= (1-t) \frac{1}{P} \sum_{i,j} p_0[i, j] + t \frac{1}{P} \sum_{i,j} p_1[i, j] \\ &= (1-t)\mu(0) + t\mu(1). \end{aligned} \quad (3)$$

Taking the expectation in the above equation, we get

$$\mathbb{E}[\mu(t)] = (1-t)\mathbb{E}[\mu(0)] + t\mathbb{E}[\mu(1)]. \quad (4)$$

Doing a similar analysis for the variance, we get,

$$\mathbb{E}[\sigma^2(t)] = \frac{1}{P} \sum_{i,j} \mathbb{E}[p_t[i, j]^2] - \mathbb{E}[\mu(t)]^2. \quad (5)$$

Next, we simplify $\mathbb{E}[p_t[i, j]^2]$ and $\mathbb{E}[\mu(t)]^2$ to get

$$\begin{aligned} \mathbb{E}[p_t^2[i, j]] &= \mathbb{E}[(1-t)^2 p_0^2[i, j] + t^2 p_1^2[i, j] \\ &\quad + 2t(1-t)p_0[i, j]p_1[i, j]] \\ &= (1-t)^2 \mathbb{E}[p_0^2[i, j]] + t^2 \mathbb{E}[p_1^2[i, j]] \\ &\quad + 2t(1-t)\mathbb{E}[p_0[i, j]p_1[i, j]], \text{ and} \end{aligned} \quad (6)$$

$$\begin{aligned} \mathbb{E}[\mu(t)]^2 &= (1-t)^2 \mathbb{E}[\mu(0)]^2 + t^2 \mathbb{E}[\mu(1)]^2 \\ &\quad + 2t(1-t)\mathbb{E}[\mu(0)]\mathbb{E}[\mu(1)]. \end{aligned} \quad (7)$$

Using expressions derived above, the expression for $\mathbb{E}[\sigma(t)]$ becomes,

$$\begin{aligned} \mathbb{E}[\sigma^2(t)] &= (1-t)^2 \left(\frac{1}{P} \sum_{i,j} \mathbb{E}[p_0^2[i, j]] - \mathbb{E}[\mu(0)]^2 \right) \\ &\quad + t^2 \left(\frac{1}{P} \sum_{i,j} \mathbb{E}[p_1^2[i, j]] - \mathbb{E}[\mu(1)]^2 \right) \\ &\quad + 2t(1-t) \left(\frac{1}{P} \sum_{i,j} \mathbb{E}[p_0[i, j]p_1[i, j]] - \mathbb{E}[\mu(0)]\mathbb{E}[\mu(1)] \right) \end{aligned} \quad (8)$$

With biological data, the image acquisition process works in the following way: a random location on the specimen slide is picked and that is then captured to generate an image frame. So, all pixel locations can be assumed to be equally likely to capture any part of any structure. We therefore assume, $\mathbb{E}[p_t[a, b]] = \mathbb{E}[p_t[c, d]] \forall a, b, c, d$ and $\mathbb{E}[p_t^2[a, b]] = \mathbb{E}[p_t^2[c, d]] \forall a, b, c, d$. So, we remove the pixel location and define p_t to be a random variable denoting a pixel in c_t . We define $\mathbb{E}[p_t] := \mathbb{E}[p_t[a, b]] \forall a, b$ and $\mathbb{E}[p_t^2] := \mathbb{E}[p_t^2[a, b]] \forall a, b$. The expression for $\mathbb{E}[\sigma(t)]$ now simplifies to,

$$\begin{aligned} \mathbb{E}[\sigma^2(t)] &= (1-t)^2 \left(\frac{1}{P} \sum_{i,j} \mathbb{E}[p_0^2] - \mathbb{E}[\mu(0)]^2 \right) \\ &\quad + t^2 \left(\frac{1}{P} \sum_{i,j} \mathbb{E}[p_1^2] - \mathbb{E}[\mu(1)]^2 \right) \\ &\quad + 2t(1-t) \left(\frac{1}{P} \sum_{i,j} \mathbb{E}[p_0 p_1] - \mathbb{E}[\mu(0)]\mathbb{E}[\mu(1)] \right) \\ &= (1-t)^2 (\mathbb{E}[p_0^2] - \mathbb{E}[\mu(0)]^2) + t^2 (\mathbb{E}[p_1^2] - \mathbb{E}[\mu(1)]^2) \\ &\quad + 2t(1-t) (\mathbb{E}[p_0 p_1] - \mathbb{E}[\mu(0)]\mathbb{E}[\mu(1)]) \\ &= (1-t)^2 \sigma(0)^2 + t^2 \sigma(1)^2 + 2t(1-t) \text{Cov}(p_0, p_1), \end{aligned} \quad (9)$$

where $\text{Cov}(\cdot, \cdot)$ is the covariance function. Now that we have the expressions for $\mathbb{E}[\mu(t)]$ and $\mathbb{E}[\sigma^2(t)]$, we consider a plausible normalization methodology where c_0 and c_1 are normalized using the following procedure: for every c_0 in C_0 , we compute its mean and standard deviation. We average the mean and standard deviation values computed over all images from C_0 to obtain a global mean and a global standard deviation. We use them to normalize every c_0 image. An identical procedure is followed for c_1 . In this case, by construction $\mathbb{E}[\mu(0)] = \mathbb{E}[\mu(1)] = 0$ and $\mathbb{E}[\sigma^2(0)] = \mathbb{E}[\sigma^2(1)] = 1$. So, from Eq. 4, $\mathbb{E}[\mu(t)] = 0$. However, $\mathbb{E}[\sigma(t)]$ still remains the following function of t ,

$$\mathbb{E}[\sigma^2(t)] = (1-t)^2 + t^2 + 2t(1-t) \text{Cov}(p_0, p_1) \quad (10)$$

As discussed in the main manuscript, this causes serious issues during normalization.

S.2. Quantitative Evaluation Methodology

In this section, we illustrate the methodology used to compute the results presented in Table 1 of the main manuscript. As an example, we describe the performance evaluation process for a specific value of w , such as $w = 0.7$. To assess a model's performance for $w = 0.7$ on a given dataset, we first generate inputs with $t = 0.3$ using Equation 1 and evaluate the performance metrics for C_0 (using Gen_0). Next, we generate inputs with $t = 0.7$ and evaluate the performance for C_1 . The average of these two metric values represents the model's overall performance for $w = 0.7$.

S.3. Normalization details for the baseline networks

The official implementations of various μ Split variants and denoiSplit are publicly available, and they share an identical input normalization scheme. During training, all pixels from images in both sub-datasets C_0 and C_1 are aggregated into a one-dimensional array, and the mean and standard deviation of this array are used to normalize all input images in the validation and test sets. It is important to note that the set of normalized patches from training data does not have a zero mean and unit standard deviation. So, similar to InDI, the optimal normalization scheme which should be employed on test images is easy to obtain.

For evaluating these baselines on the tasks presented in Table 1, we adhere to their normalization scheme with one modification: for each mixing ratio t , the mean and standard deviation are computed using pixels exclusively from the input images c_t . Note that when evaluating test images, we cannot assume access to individual channels and so cannot use their normalization scheme. Note that this scheme is applied solely to these baselines during evaluation.

S.4. Hyper-parameters and training details

We use a patch size of 512 to train indiSplit, InDI, U-Net and denoiSplit networks. For μ Split variants, we kept the patch size as 64, which is used in their official implementation. The reason is that, in spite of using 64 as the patch size, they effectively see the content of 1024×1024 sized region surrounding the primary input patch. This is because of the presence of the LC module they have in their network which takes as input additional low-resolution patches centered on the primary patch but spanning larger and larger spatial regions. For training Gen_i networks, we use MAE loss and for training Reg network, we use MSE loss. We use Adam optimizer with a learning rate of $1e-3$. To have a fair comparison between InDI and indiSplit, we used the same parameter count, non-linearity, number of layers *etc.* between them. We used MMSE-count of 10 to compute all metrics. In other words, for every input, we predicted 10 times, and used the average prediction for metric computation. All metric computation has been done on predictions of entire frames (and not on patches).

For Hagen et al. dataset, to allow all methods to compare with pretrained models of μ Split variants, we followed μ Split code of applying upper-clip to the data at 0.995 quantile. We upper-clipped the data at intensity value of 1993. This corresponds to 0.995 quantile of the entire training data. Similarly, for PaviaATN, the upper-clipping operation was done at 1308 value.

GT	Mean	Median	Mode	WgtSum	WgtProd
0.00	0.13	0.12	0.11	0.14	0.15
0.10	0.15	0.14	0.10	0.16	0.16
0.20	0.21	0.20	0.13	0.20	0.20
0.30	0.31	0.28	0.27	0.29	0.27
0.40	0.43	0.41	0.35	0.42	0.40
0.50	0.54	0.53	0.66	0.54	0.51
0.60	0.64	0.64	0.61	0.63	0.61
0.70	0.72	0.72	0.74	0.71	0.69
0.80	0.77	0.78	0.79	0.77	0.76
0.90	0.80	0.79	0.78	0.79	0.80
1.00	0.80	0.80	0.78	0.80	0.81

Table S.1. Quantitative evaluation of different aggregation methodologies on BioSR data. First column is the ground truth t and all other columns are the aggregated predictions using different aggregation methodologies.

S.5. Different aggregation methodologies

In this section, we experiment with different ways to aggregate the estimates of the mixing-ratio t . We iterate over the test set and for each patch, we get an estimate of t . We tried several ways to aggregate the estimates. We aggregated the estimates using mean, median and mode as three different ways. Next, building on the hypothesis that the estimates of patches containing both structures might be better, we implemented two more aggregation methods. We replicate the scalar mixing-ratio predictions to have the same shape as the input patches. We then tile these replicated mixing-ratio predictions so that, they have the same shape as the full input frames. Using $t = 0.5$, we first make a rough estimate of both channels, \hat{c}_0 and \hat{c}_1 . We then take the weighted average of the tiled replicated mixing-ratios, with weights computed by normalizing (a) $\hat{c}_0 + \hat{c}_1$ and (b) $\hat{c}_0 * \hat{c}_1$. We call them $WgtSum$ and $WgtProd$. We do not observe any significant advantage for any of the above mentioned aggregation methods in Tables S.1, S.2 and S.3 and so we resort to using mean as our aggregation method on all tasks.

S.6. On design of Gen_i

As described in the main text, we worked with a setup which requires one generator network per channel. While one can envisage an alternative implementation using a single generative network with two channels instead of two separate networks Gen_0 and Gen_1 , extending it to multiple channels with each channel contributing differently to the input, which is our future goal, would become complicated and so we decided on this cleaner design.

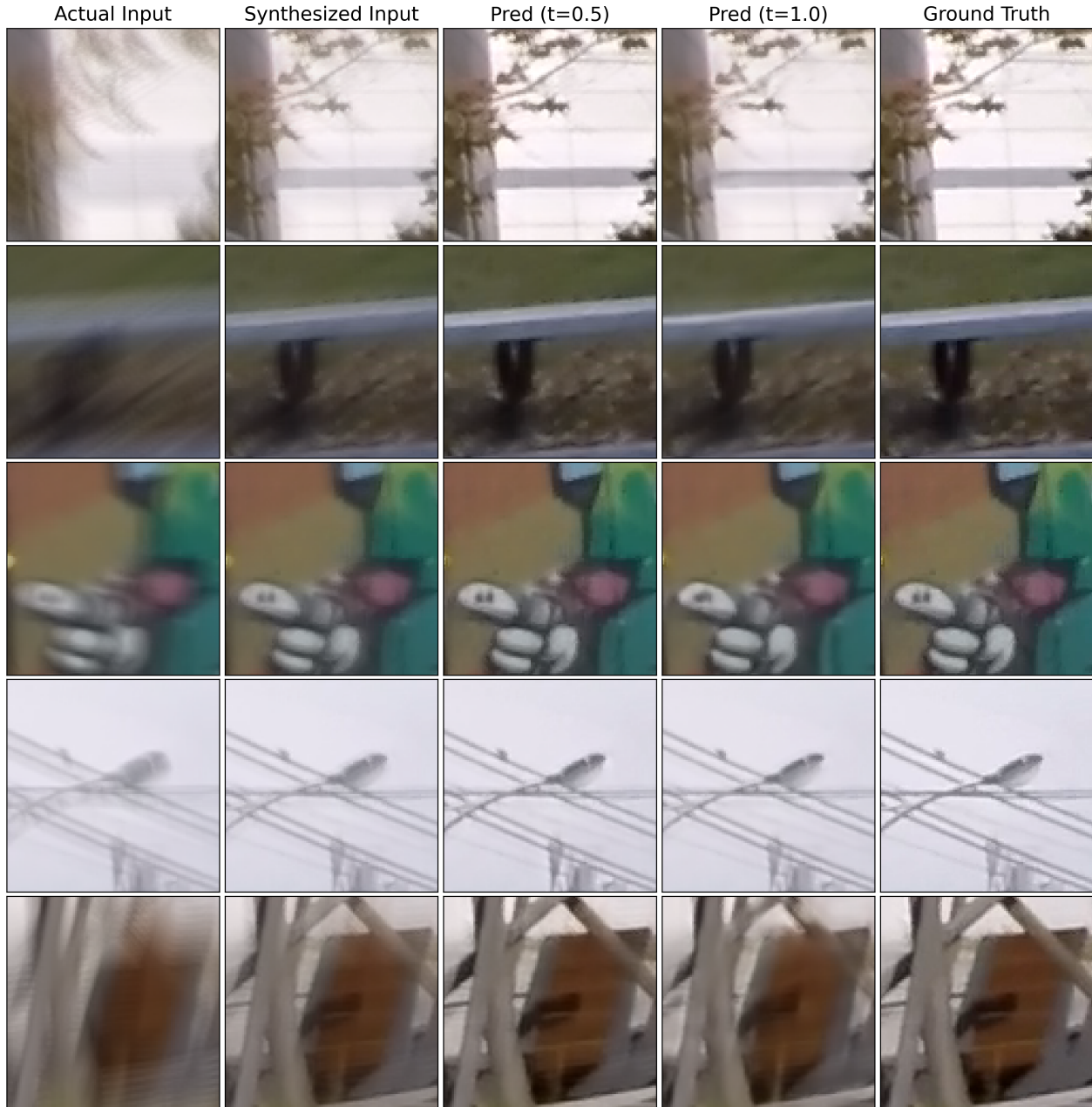


Figure S.1. Here, we qualitatively show the potential benefit of regulating the restoration process by making the network cognizant to severity of degradation present in the input image. Predictions are made on ‘Synthesized Input’, which is created by doing the pixelwise average of Actual Input and the ground truth image. This essentially yields a less blurry image. In the reference frame of the trained `indiSplit`, $t = 0.5$ would be the optimal inference setting for these synthesized inputs. We cherry picked few 100×100 size crops where the difference between the prediction made by `indiSplit` with $t = 0.5$ and with $t = 1.0$ was clearly visible. We also show quantitative evaluation on all similarly synthesized input frames from the test sub-dataset in Table S.4.

S.7. Application to natural images

For image restoration tasks, it is evident that in reality, images with different levels of degradation exist and therefore, a method that is cognizant of the severity of degradation is

expected to have advantages.

However, to make our idea applicable to image restoration tasks on natural images, one would need to account for the differences between the image unmixing task performed on microscopy data and those tasks. For example, in fluo-

GT	Mean	Median	Mode	WgtSum	WgtProd
0.00	0.13	0.10	0.09	0.11	0.11
0.10	0.14	0.12	0.10	0.12	0.12
0.20	0.25	0.23	0.22	0.22	0.24
0.30	0.35	0.35	0.35	0.34	0.36
0.40	0.45	0.45	0.46	0.45	0.46
0.50	0.53	0.54	0.54	0.53	0.55
0.60	0.61	0.62	0.64	0.61	0.63
0.70	0.69	0.70	0.71	0.69	0.71
0.80	0.78	0.80	0.79	0.78	0.80
0.90	0.87	0.89	0.87	0.86	0.87
1.00	0.92	0.96	0.96	0.93	0.92

Table S.2. Quantitative evaluation of different aggregation methodologies on HTT24 data. First column is the ground truth t and all other columns are the aggregated predictions using different aggregation methodologies.

GT	Mean	Median	Mode	WgtSum	WgtProd
0.00	0.13	0.11	0.09	0.13	0.13
0.10	0.18	0.16	0.14	0.18	0.18
0.20	0.24	0.22	0.17	0.24	0.24
0.30	0.34	0.33	0.26	0.32	0.32
0.40	0.43	0.42	0.44	0.40	0.40
0.50	0.52	0.51	0.52	0.49	0.48
0.60	0.60	0.58	0.57	0.56	0.56
0.70	0.69	0.68	0.61	0.66	0.65
0.80	0.78	0.78	0.76	0.76	0.75
0.90	0.87	0.88	0.88	0.88	0.87
1.00	0.89	0.90	0.90	0.91	0.90

Table S.3. Quantitative evaluation of different aggregation methodologies on HTLIF24 data. First column is the ground truth t and all other columns are the aggregated predictions using different aggregation methodologies.

$t_{assumed}$	PSNR
0.3	35.0
0.5	37.3
0.7	36.2
1.0	32.4

Table S.4. Evaluating performance of indiSplit on synthetic inputs created from the test sub-dataset of GoPro motion deblurring dataset. Informally speaking, half of the haze was removed from the original test images using Equation 11. indiSplit indeed was able to yield superior performance when t was set to 0.5 during inference.

rescence microscopy, we made a plausible assumption that a single acquisition amounts to a single mixing-ratio. However, in a motion deblurring task, the portion of the image

containing a moving object, *e.g.* a car, will have more severe blurring when compared to a static object, like a wall. So, one would need to account for this spatial variation of the degradation. For de-hazing and de-raining tasks, a similar challenge holds. Objects more distant from the camera typically have more degradation. So, to handle such spatially varying degradations in a diligent manner, t , the input to indiSplit also needs to be spatially varying and therefore should not remain a scalar. Secondly, for the image unmixing task described in this work, we have access to the two channels, and so we can correctly define the mixing-ratio. However, with these image restoration tasks, one does not have access to the other channel, which would be pure degradation. One instead has access to the clean content and an intermediately degraded image. So, $t = 1$ will have different connotations for the image-unmixing task described in this work and image restoration tasks on natural images, which need to be properly accounted for.

However, as a proof of concept, we trained indiSplit with just one generator network Gen_0 for the motion deblurring task on GoPro motion deblurring dataset [22]. Since all the variations of severity of degradation present in the training data were explicitly mapped to $t = 1$ during training (all degraded images belong to C_1 , which means $t = 1$ for all such images and this is irrespective of their qualitative degradation levels), it is expected that during inference, $t = 1$ will be the optimum choice on the test sub-dataset provided in this dataset.

So, to enhance the diversity of the degradation, we took the test set of the GoPro dataset and created a set of less degraded input images, by simply averaging the inputs with the respective targets *i.e.*,

$$x_{new}^i = 0.5x^i + 0.5y^i, \quad (11)$$

where x^i is the original input image and y^i is the corresponding target image. Next, we evaluate the indiSplit network on all x_{new}^i images while using different values of t during inference. We show the results in Table S.4 and the qualitative results in Figure S.1.

In this case, one indeed observes that $t = 0.5$ is the optimal choice. Interestingly, even slightly off estimates of t ($t = 0.3$, and $t = 0.7$) also yield superior performance over $t = 1.0$. This proof-of-concept experiment shows that when handling blurry images with lower levels of degradation, $t = 1$ is not an optimal choice. But due to the non-trivial differences between our current image unmixing task and these restoration tasks, as outlined above, we plan to take up the task of adapting indiSplit for natural images in a separate work.

S.8. Analyzing the Effect of Precision

In the official configuration of μ Split variants, we found that the training was done with 16 bit floating point precision.

The pre-trained models for μ Split are also trained with 16 bit precision. However, other baselines and indiSplit are trained with 32 bit precision. So, we trained μ Split_L with 32 bit precision to assess the performance difference. We compare the performance in Table S.5. Across the three input regimes, one observes the average PSNR increment of 0.3db, MS-SSIM increment of 0.002 and LPIPS decrement of 0.004 when one uses 32 bit floating point precision. By observing Table 1, it is evident that this change is much smaller than the advantage indiSplit has across all three input regimes.

S.9. Qualitative Performance Evaluation

For different values of w , we show the qualitative results for the Hagen et al. dataset in Figures S.3, S.4 and S.5. For the BioSR dataset, results are shown in Figures S.6, S.7 and S.8. For the HTT24 dataset, results are shown in Figures S.9, S.10 and S.11. For the HTLIF24 dataset, results are shown in Figures S.12, S.13 and S.14. For the PaviaATN dataset, results are shown in Figures S.15, S.16 and S.17.

	Dominant			Balanced			Weak		
	PSNR	SSIM	LPIPS	PSNR	SSIM	LPIPS	PSNR	SSIM	LPIPS
μSplit_L (16-bit)	37.8	0.918	0.066	33.5	0.959	0.051	25.7	0.738	0.291
μSplit_L (32-bit)	38.1	0.918	0.065	33.9	0.962	0.045	25.9	0.741	0.284

Table S.5. Analysing the effect of training with 32 bit vs. training with 16 bit floating point precision. In μSplit variants, the official configuration is to train with 16 bit floating point precision.

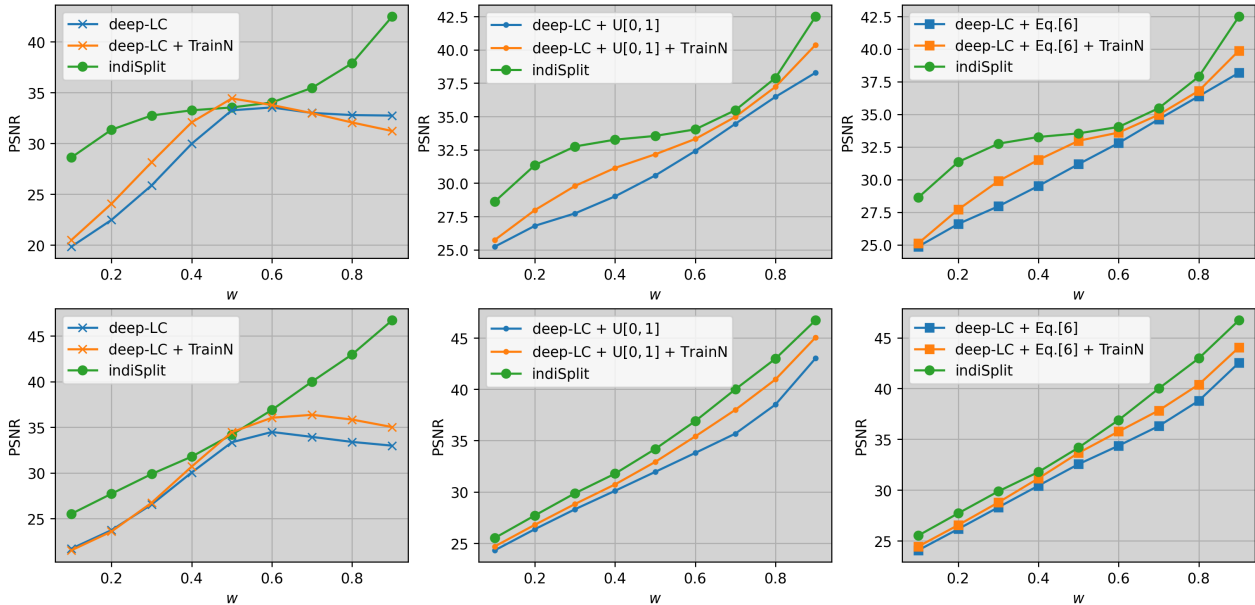


Figure S.2. This figure investigates the influence of normalization on the performance of μSplit_D , emphasizing its inferior outcomes relative to indiSplit . Notably, other μSplit variants and denoSplit share the same normalization setup as μSplit_D , making this analysis broadly applicable to several existing unmixing methods. We evaluate μSplit_D and two of its variants, each utilizing distinct augmentation strategies, as outlined in the main manuscript’s Fig 5. Performance is assessed under two normalization schemes: (1) the default approach, where mean and standard deviation are derived from the training data, and (2) a w -dependent method, where statistics are calculated separately for inputs with a specific w . The results demonstrate that all μSplit_D variants underperform compared to indiSplit under both normalization strategies. Furthermore, we note that μSplit_D , trained with uniform normalization statistics, performs more effectively under the default evaluation setup, which as discussed in the main manuscript is not a reasonable choice given the intensity variations across different microscopy acquisitions.

Dataset		Dominant			Balanced			Weak		
		PSNR	SSIM	LPIPS	PSNR	SSIM	LPIPS	PSNR	SSIM	LPIPS
Hagen et. al	Inp vs Tar	34.1	0.973	0.047	25.1	0.889	0.148	21.2	0.784	0.243
	U-Net	33.5	0.976	0.038	33.4	0.960	0.066	23.3	0.840	0.190
	μSplit_L	34.2	0.974	0.044	32.3	0.959	0.071	23.8	0.843	0.187
	μSplit_R	34.6	0.971	0.041	32.4	0.957	0.068	24.5	0.842	0.189
	μSplit_D	33.9	0.975	0.039	33.6	0.963	0.061	24.1	0.849	0.179

Table S.6. This table, analogous to Table 1 in the main manuscript, evaluates performance on the Hagen et al. dataset across the same three input categories. Here, we utilize the mean and standard deviation computed from the training data for normalization. Since μSplit variants are trained with these statistics, they achieve superior performance with this normalization setting, since the test images share the same intensity distribution as the training data due to being from the same acquisition. However, as outlined in the main manuscript, this approach is not viable for evaluating images from different acquisitions, where intensity distributions may vary. Notably, indiSplit surpasses even these results, demonstrating its robustness and superior performance.

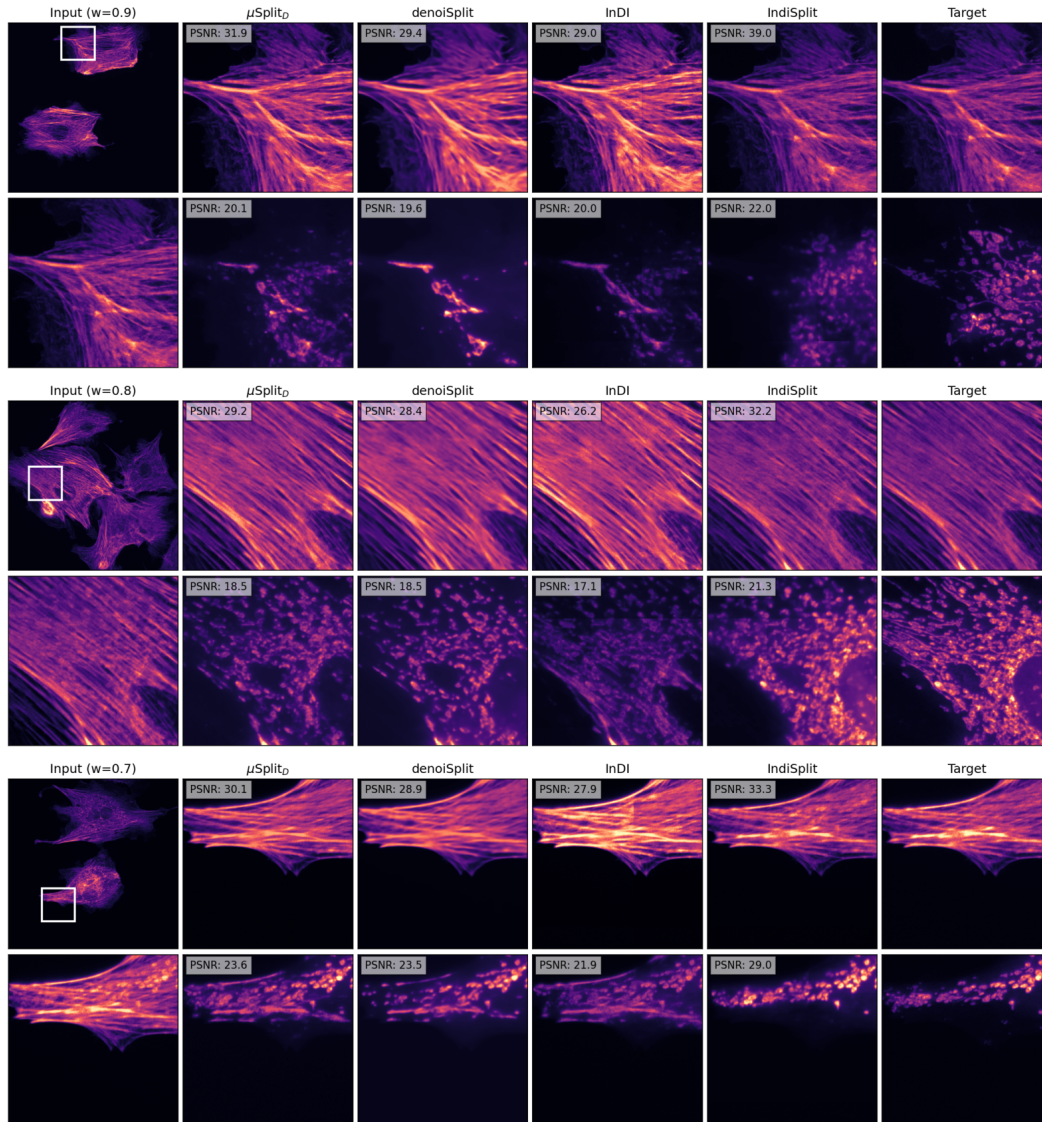


Figure S.3. Qualitative evaluation for Hagen et al. In each panel, we show the full input frame (top-left) and the zoomed-in input patch (bottom-left) for which we show the predictions and the targets (last col) for the two channels, one in each row. We also report PSNR values for the patch shown. The w value reported on top of the input column is for the first channel. It naturally becomes $1 - w$ for the second channel.

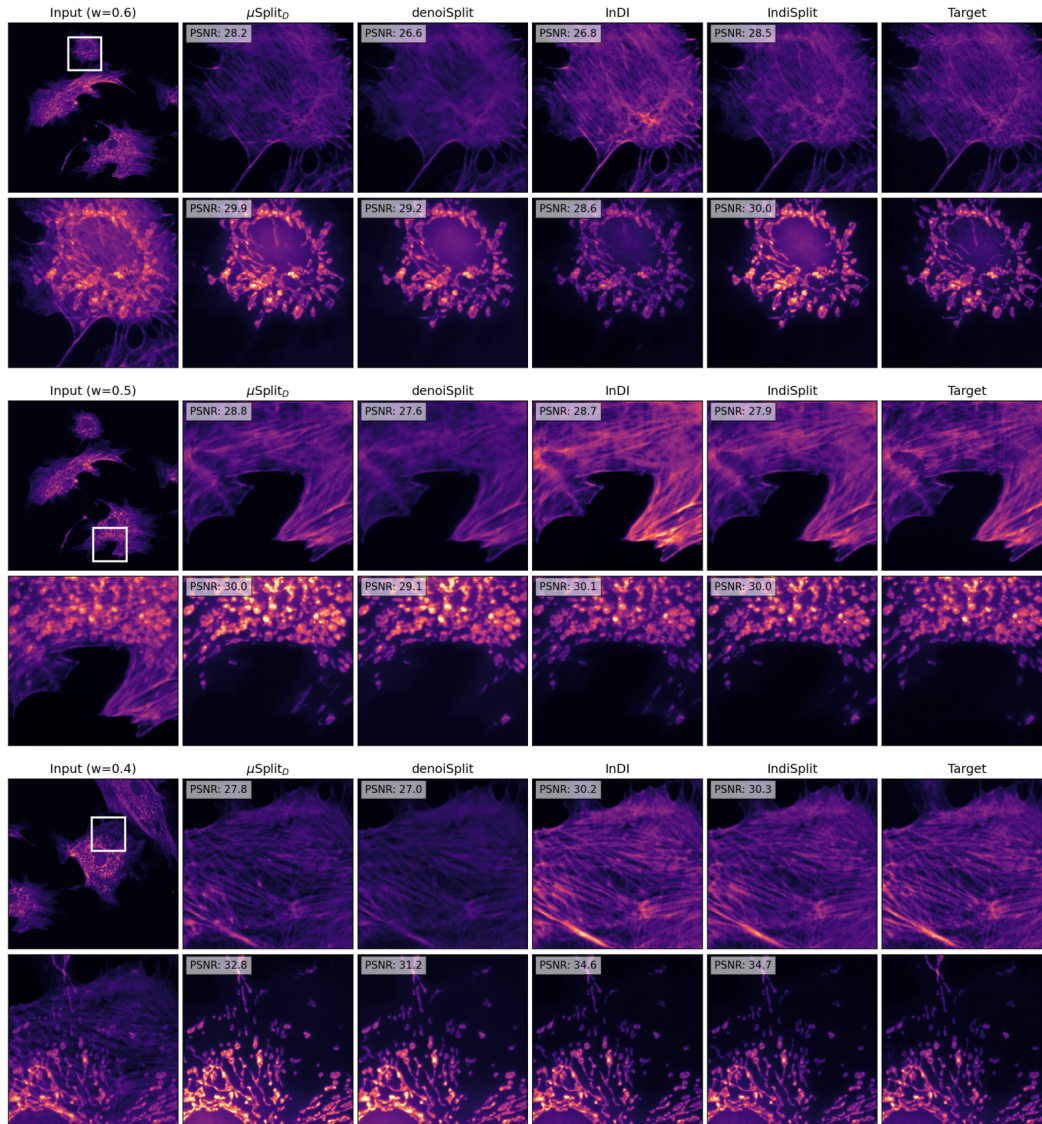


Figure S.4. Qualitative evaluation for Hagen et al. In each panel, we show the full input frame (top-left) and the zoomed-in input patch (bottom-left) for which we show the predictions and the targets (last col) for the two channels, one in each row. We also report PSNR values for the patch shown. The w value reported on top of the input column is for the first channel. It naturally becomes $1 - w$ for the second channel.

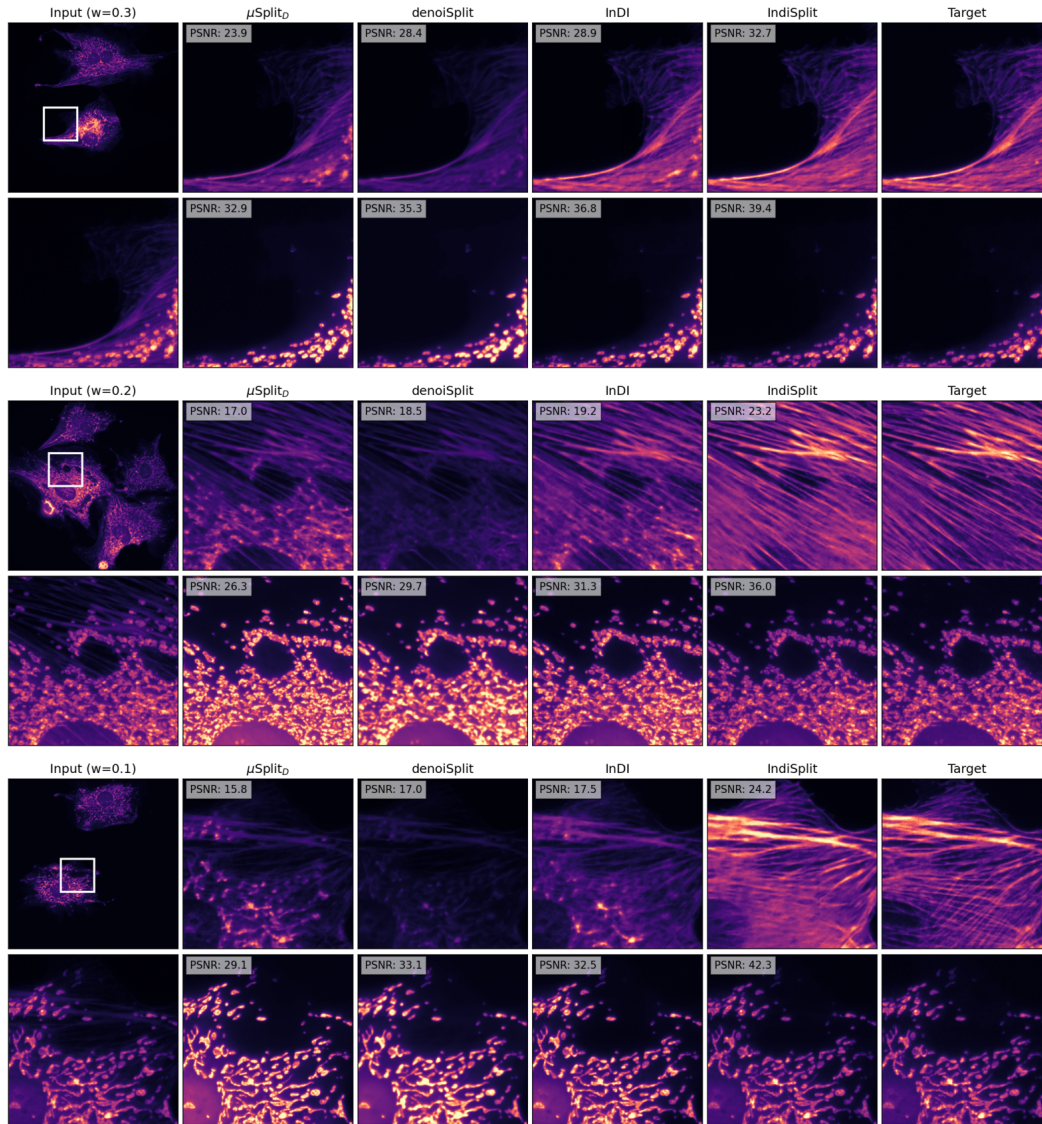


Figure S.5. Qualitative evaluation for Hagen et al. In each panel, we show the full input frame (top-left) and the zoomed-in input patch (bottom-left) for which we show the predictions and the targets (last col) for the two channels, one in each row. We also report PSNR values for the patch shown. The w value reported on top of the input column is for the first channel. It naturally becomes $1 - w$ for the second channel.

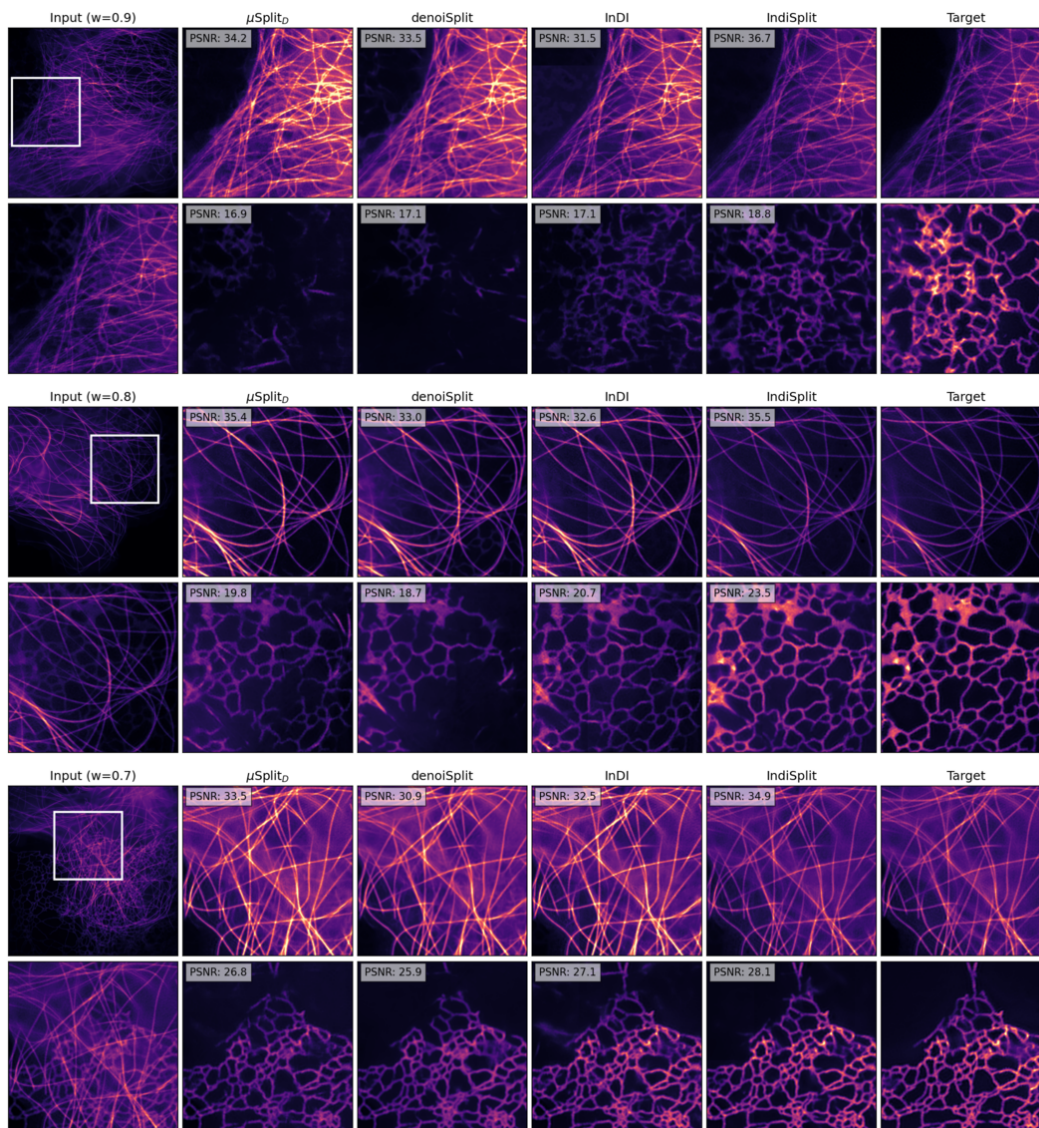


Figure S.6. Qualitative evaluation for BioSR dataset. In each panel, we show the full input frame (top-left) and the zoomed-in input patch (bottom-left) for which we show the predictions and the targets (last col) for the two channels, one in each row. We also report PSNR values for the patch shown. The w value reported on top of the input column is for the first channel. It naturally becomes $1 - w$ for the second channel.

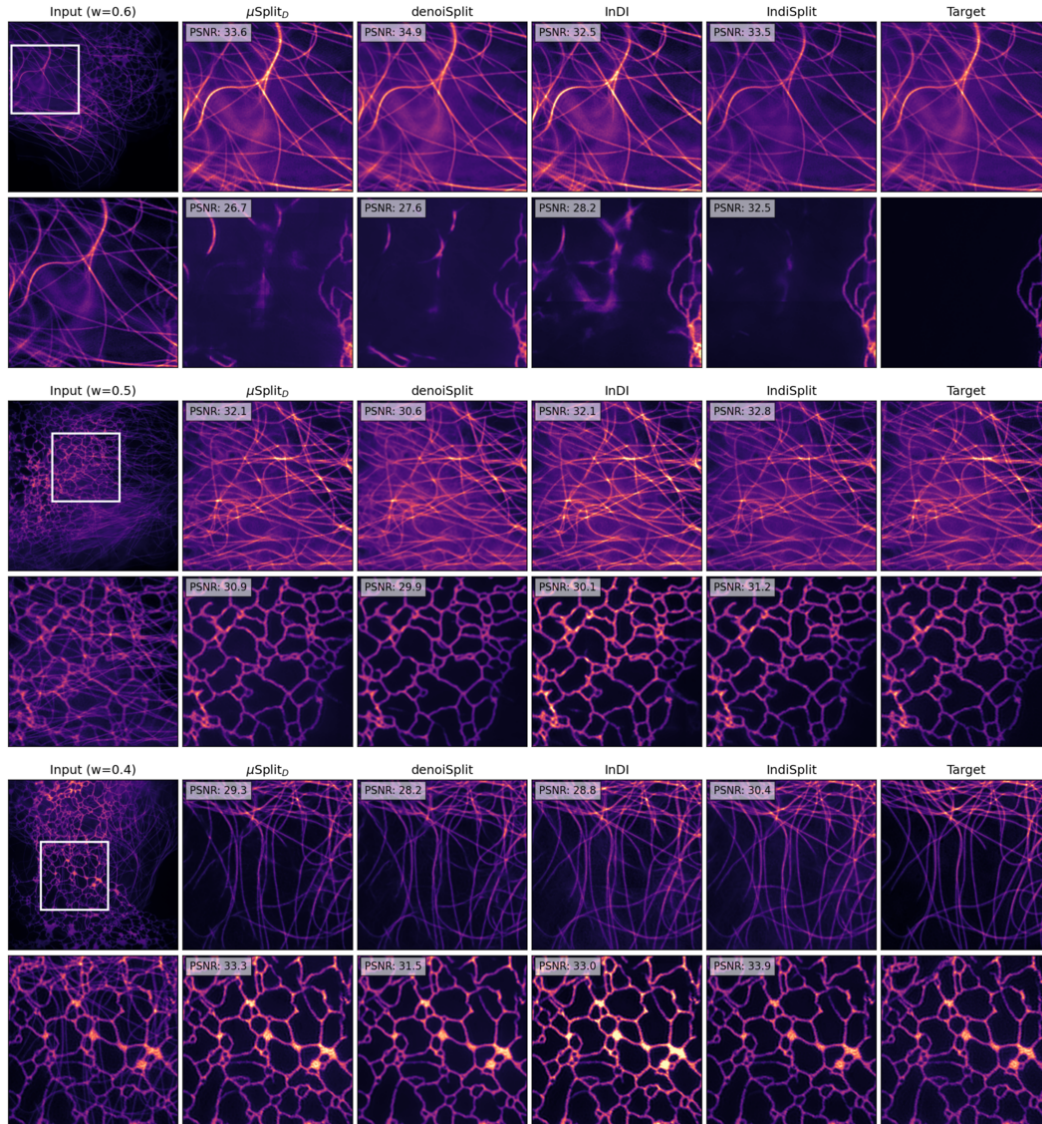


Figure S.7. Qualitative evaluation for BioSR dataset. In each panel, we show the full input frame (top-left) and the zoomed-in input patch (bottom-left) for which we show the predictions and the targets (last col) for the two channels, one in each row. We also report PSNR values for the patch shown. The w value reported on top of the input column is for the first channel. It naturally becomes $1 - w$ for the second channel.

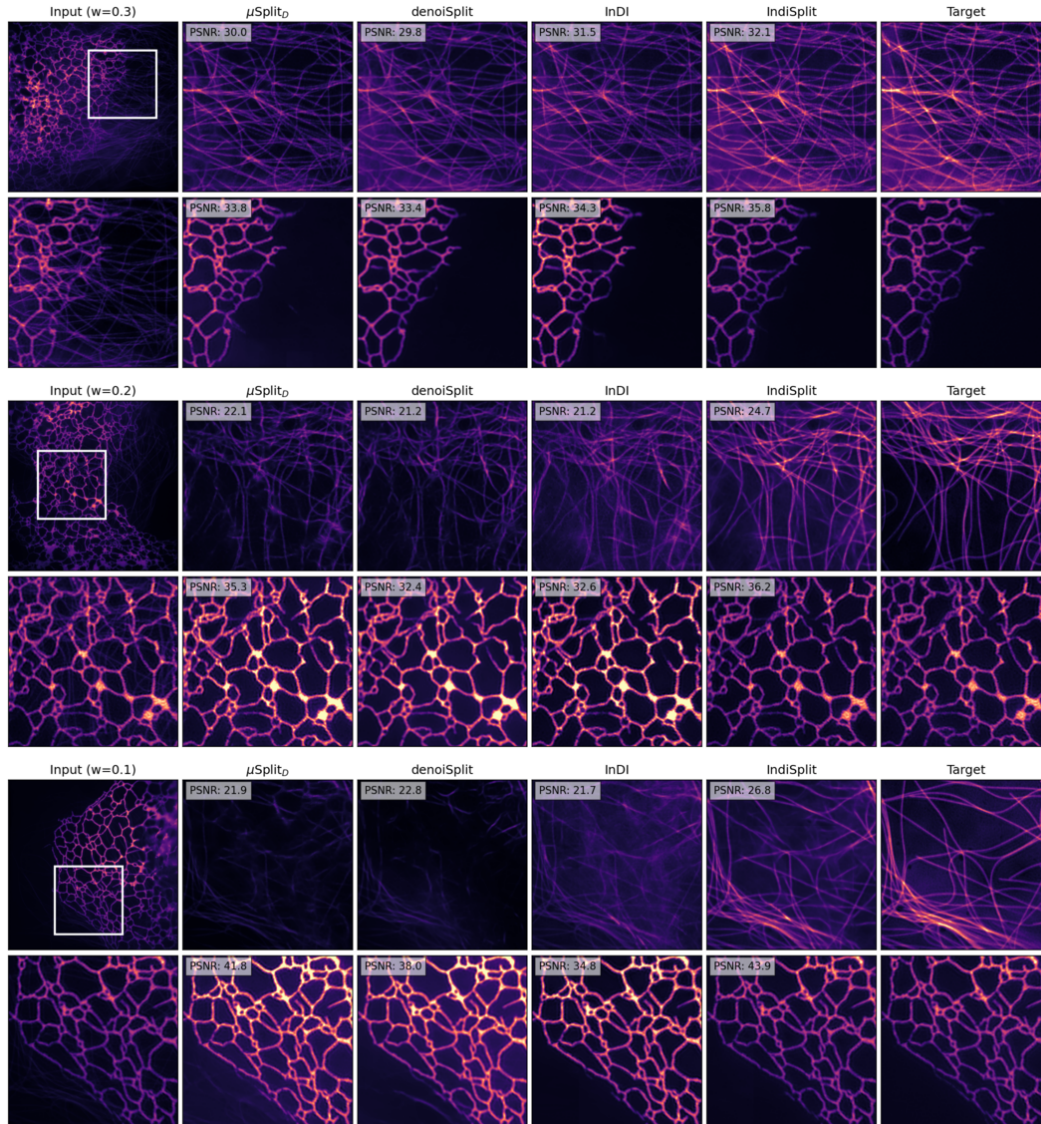


Figure S.8. Qualitative evaluation for BioSR dataset. In each panel, we show the full input frame (top-left) and the zoomed-in input patch (bottom-left) for which we show the predictions and the targets (last col) for the two channels, one in each row. We also report PSNR values for the patch shown. The w value reported on top of the input column is for the first channel. It naturally becomes $1 - w$ for the second channel.

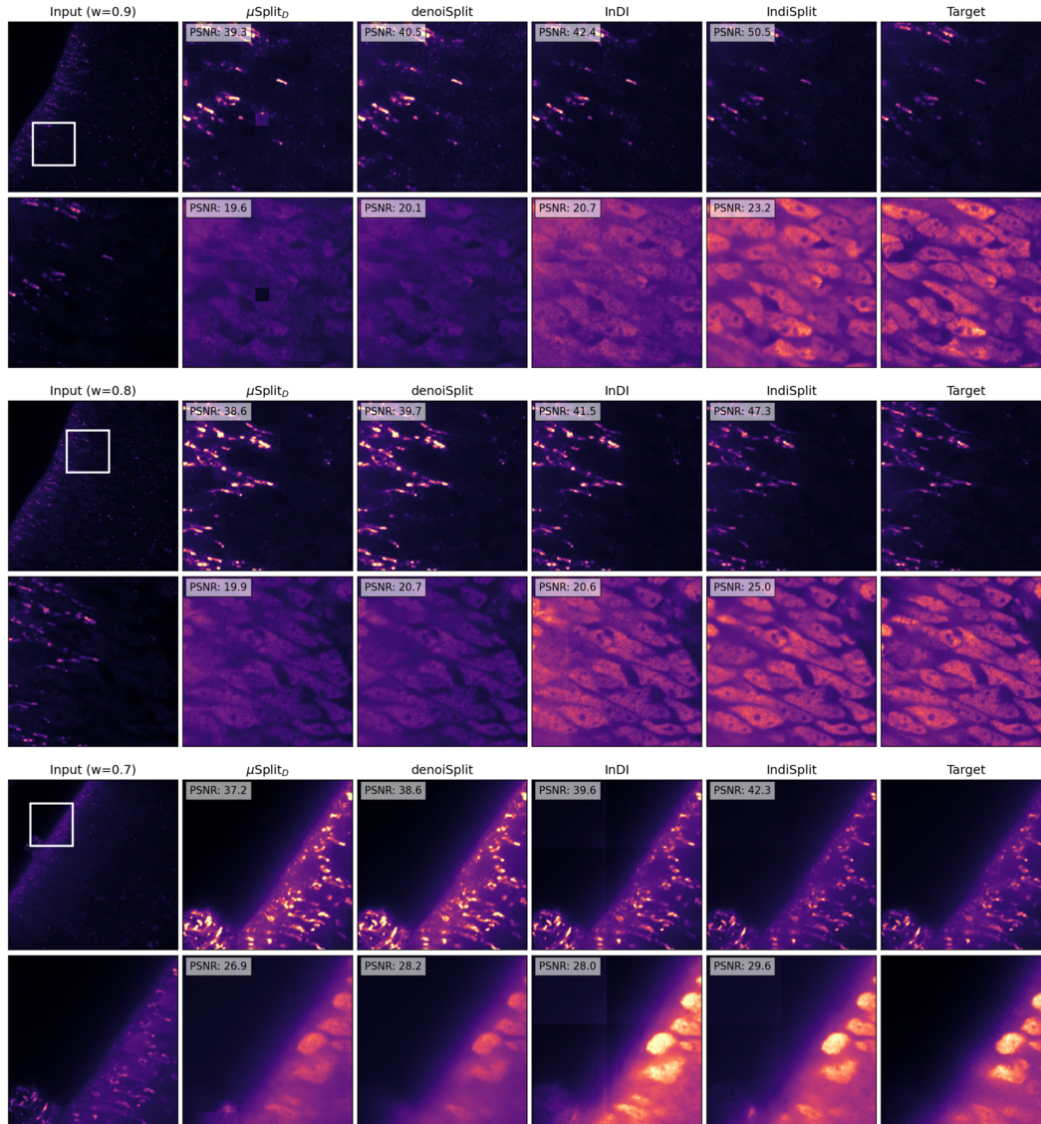


Figure S.9. Qualitative evaluation for HTT24 dataset. In each panel, we show the full input frame (top-left) and the zoomed-in input patch (bottom-left) for which we show the predictions and the targets (last col) for the two channels, one in each row. We also report PSNR values for the patch shown. The w value reported on top of the input column is for the first channel. It naturally becomes $1 - w$ for the second channel.

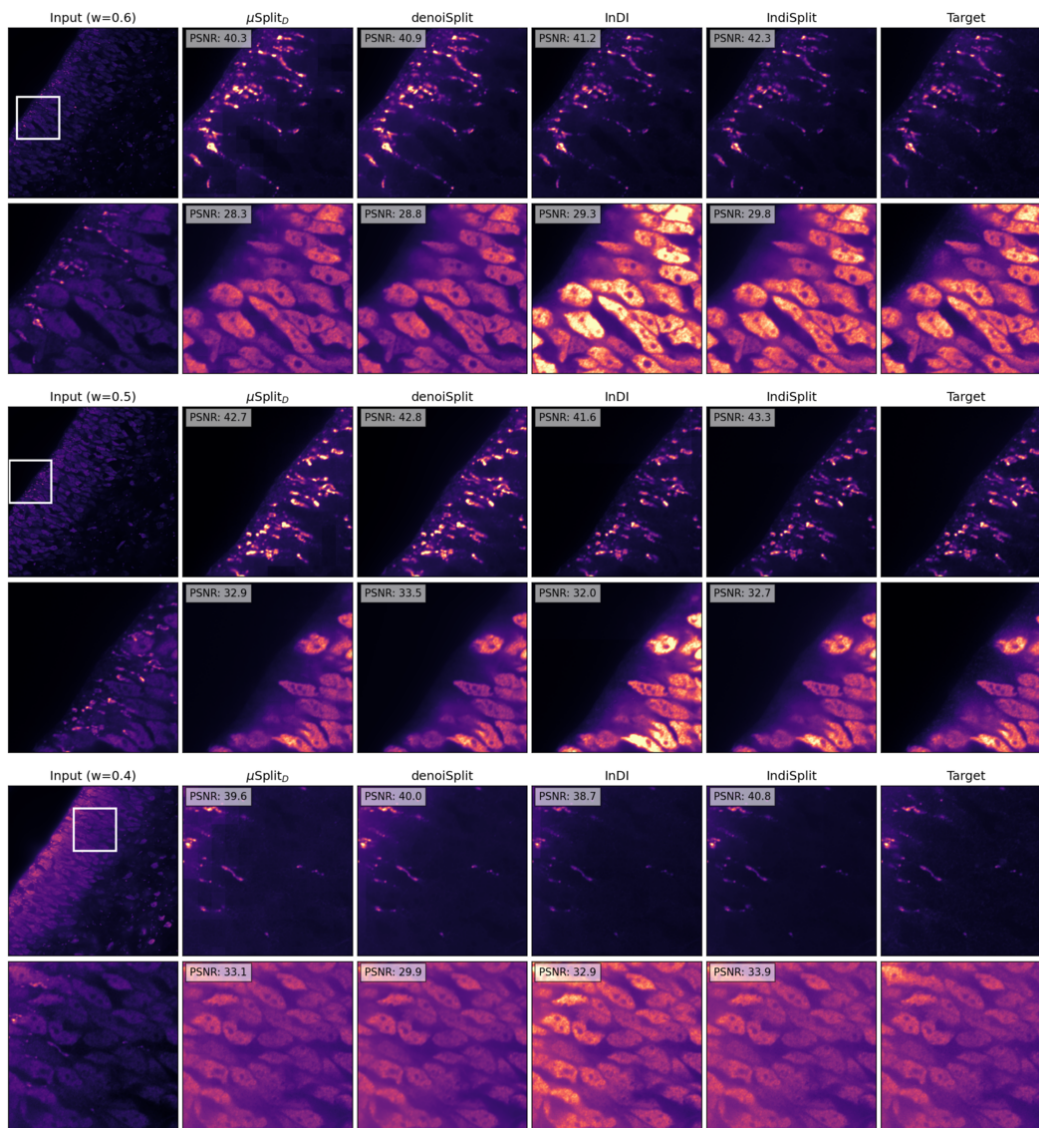


Figure S.10. Qualitative evaluation for HTT24 dataset. In each panel, we show the full input frame (top-left) and the zoomed-in input patch (bottom-left) for which we show the predictions and the targets (last col) for the two channels, one in each row. We also report PSNR values for the patch shown. The w value reported on top of the input column is for the first channel. It naturally becomes $1 - w$ for the second channel.

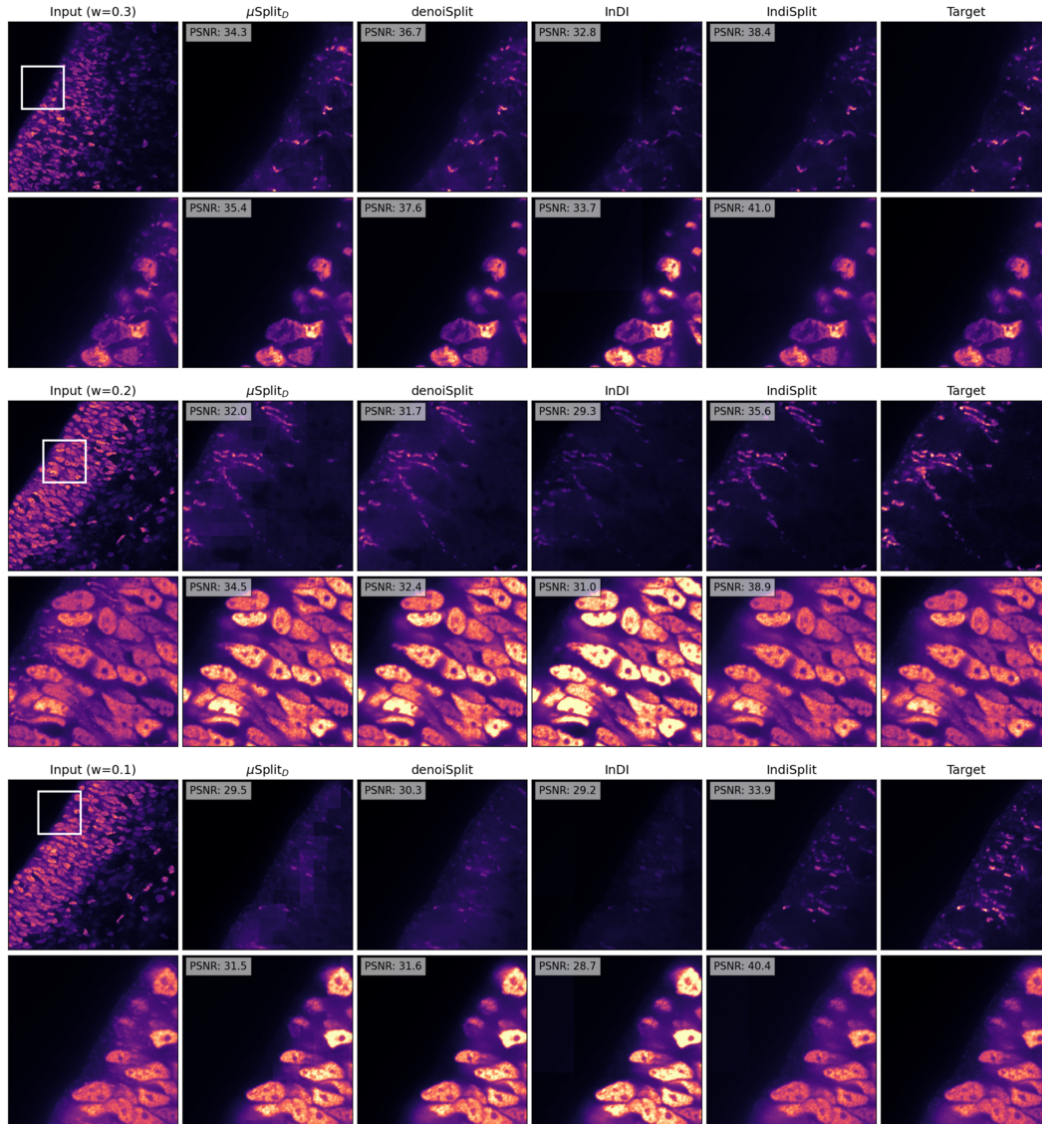


Figure S.11. Qualitative evaluation for HTT24 dataset. In each panel, we show the full input frame (top-left) and the zoomed-in input patch (bottom-left) for which we show the predictions and the targets (last col) for the two channels, one in each row. We also report PSNR values for the patch shown. The w value reported on top of the input column is for the first channel. It naturally becomes $1 - w$ for the second channel.

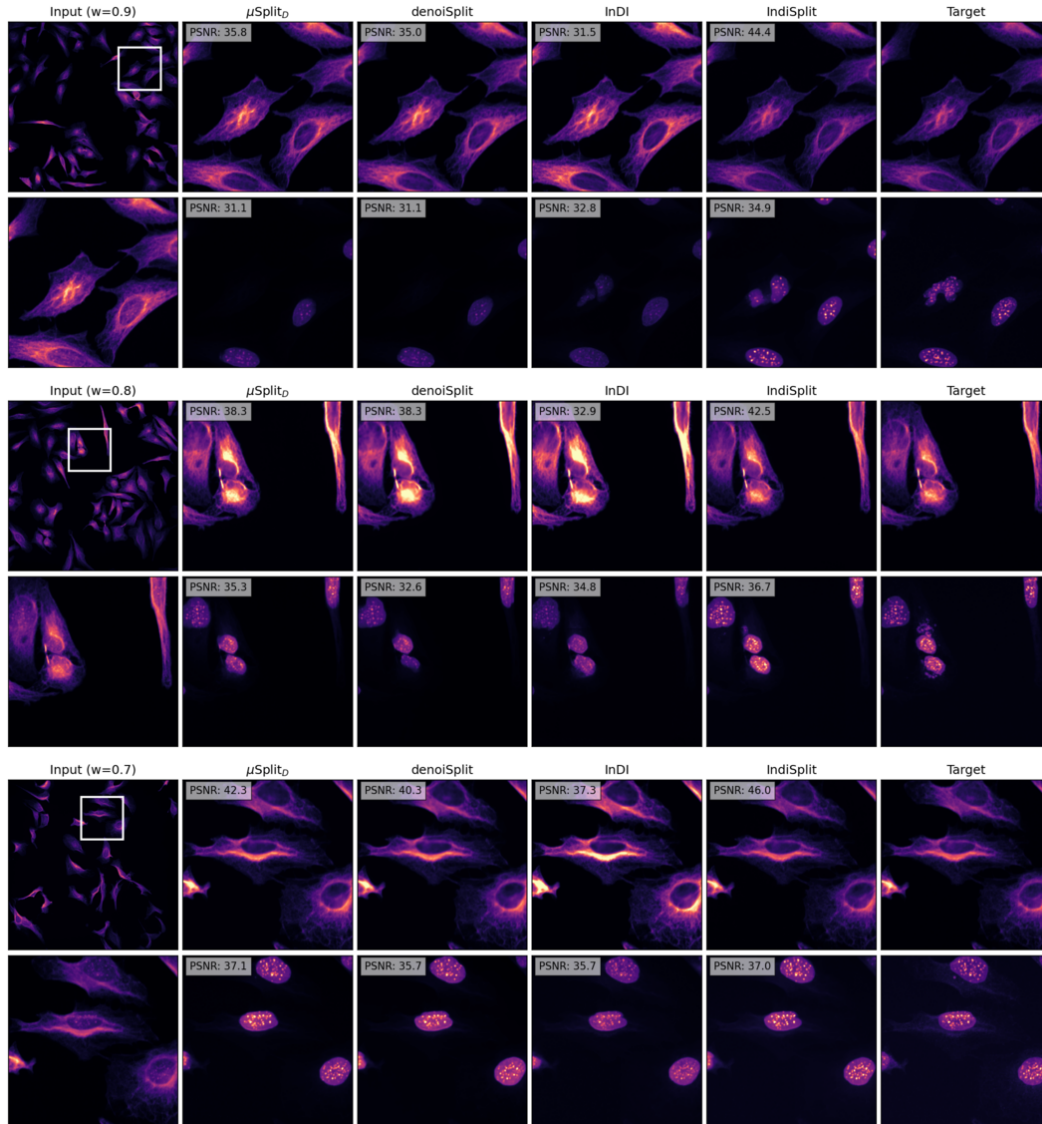


Figure S.12. Qualitative evaluation for HTLIF24 dataset. In each panel, we show the full input frame (top-left) and the zoomed-in input patch (bottom-left) for which we show the predictions and the targets (last col) for the two channels, one in each row. We also report PSNR values for the patch shown. The w value reported on top of the input column is for the first channel. It naturally becomes $1 - w$ for the second channel.

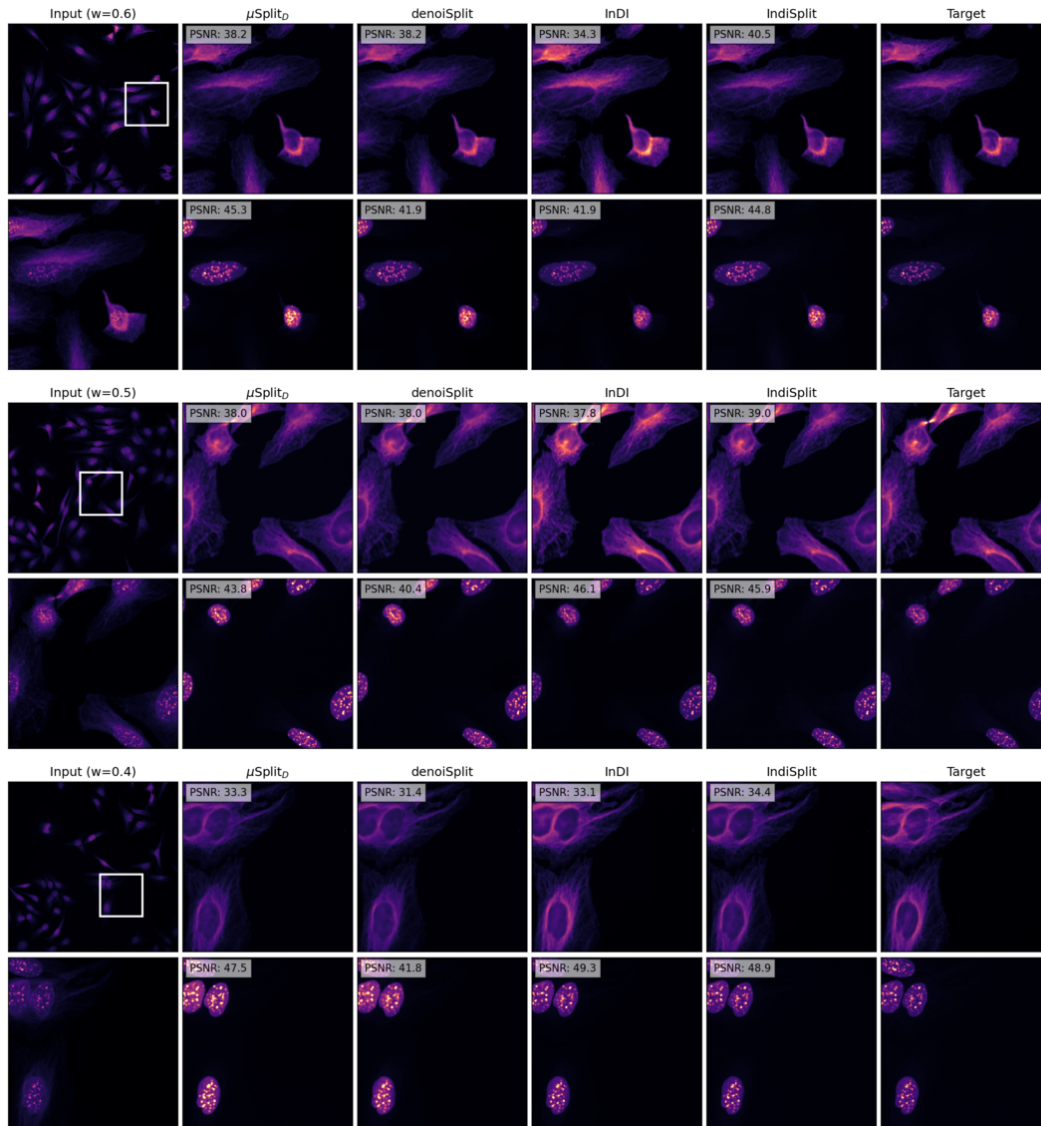


Figure S.13. Qualitative evaluation for HTLIF24 dataset. In each panel, we show the full input frame (top-left) and the zoomed-in input patch (bottom-left) for which we show the predictions and the targets (last col) for the two channels, one in each row. We also report PSNR values for the patch shown. The w value reported on top of the input column is for the first channel. It naturally becomes $1 - w$ for the second channel.

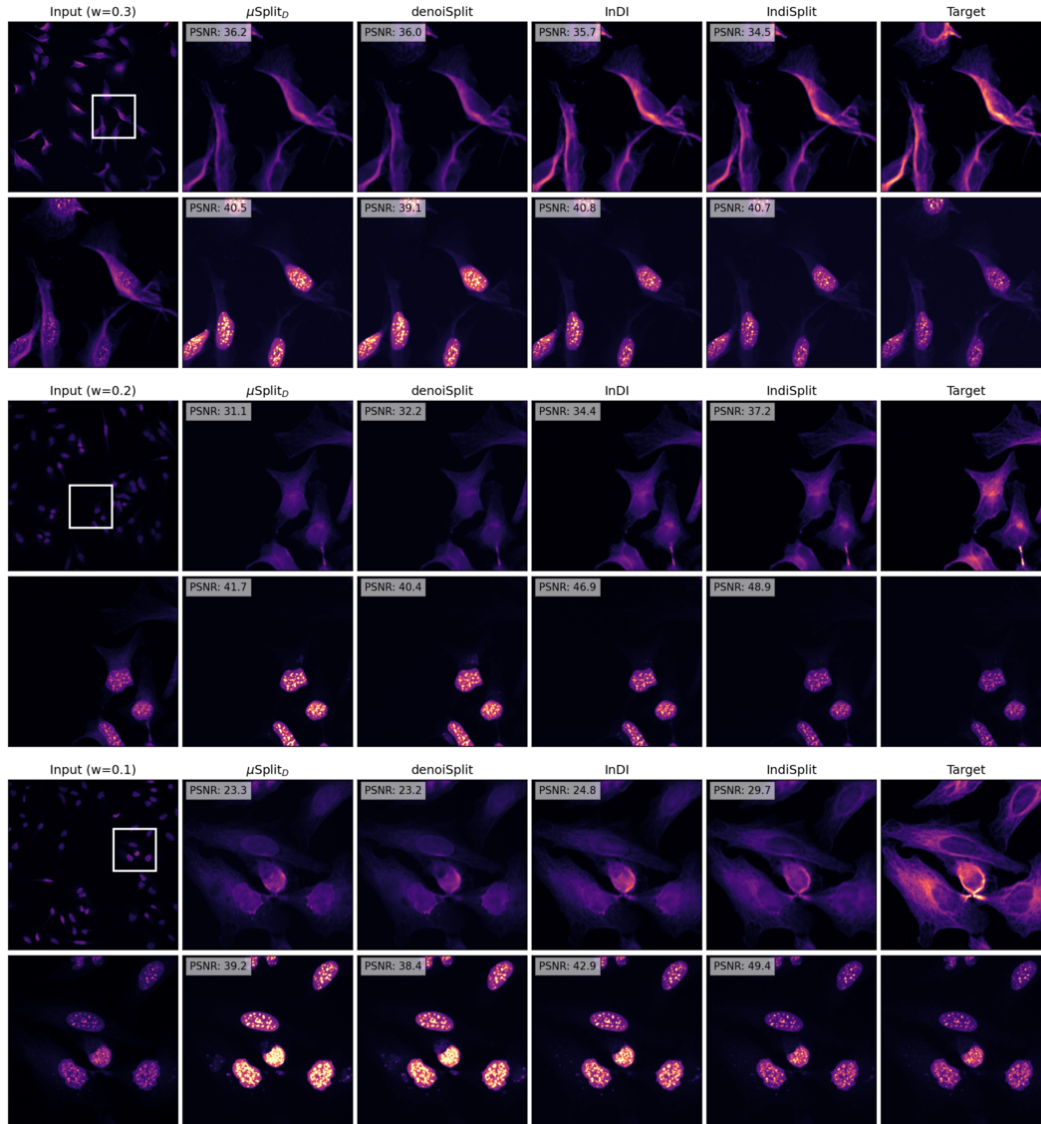


Figure S.14. Qualitative evaluation for HTLIF24 dataset. In each panel, we show the full input frame (top-left) and the zoomed-in input patch (bottom-left) for which we show the predictions and the targets (last col) for the two channels, one in each row. We also report PSNR values for the patch shown. The w value reported on top of the input column is for the first channel. It naturally becomes $1 - w$ for the second channel.

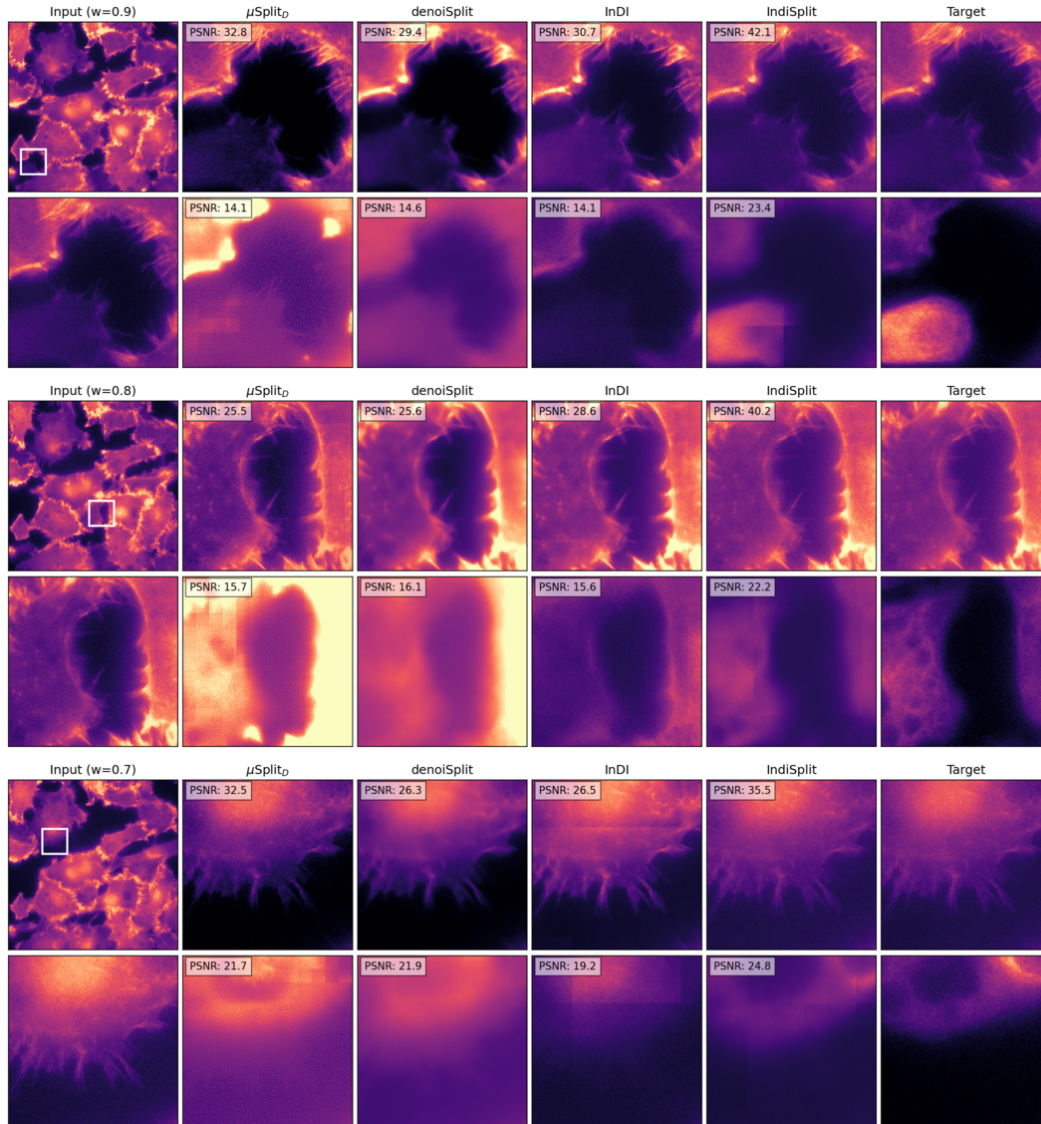


Figure S.15. Qualitative evaluation for PaviaATN dataset. In each panel, we show the full input frame (top-left) and the zoomed-in input patch (bottom-left) for which we show the predictions and the targets (last col) for the two channels, one in each row. We also report PSNR values for the patch shown. The w value reported on top of the input column is for the first channel. It naturally becomes $1 - w$ for the second channel.

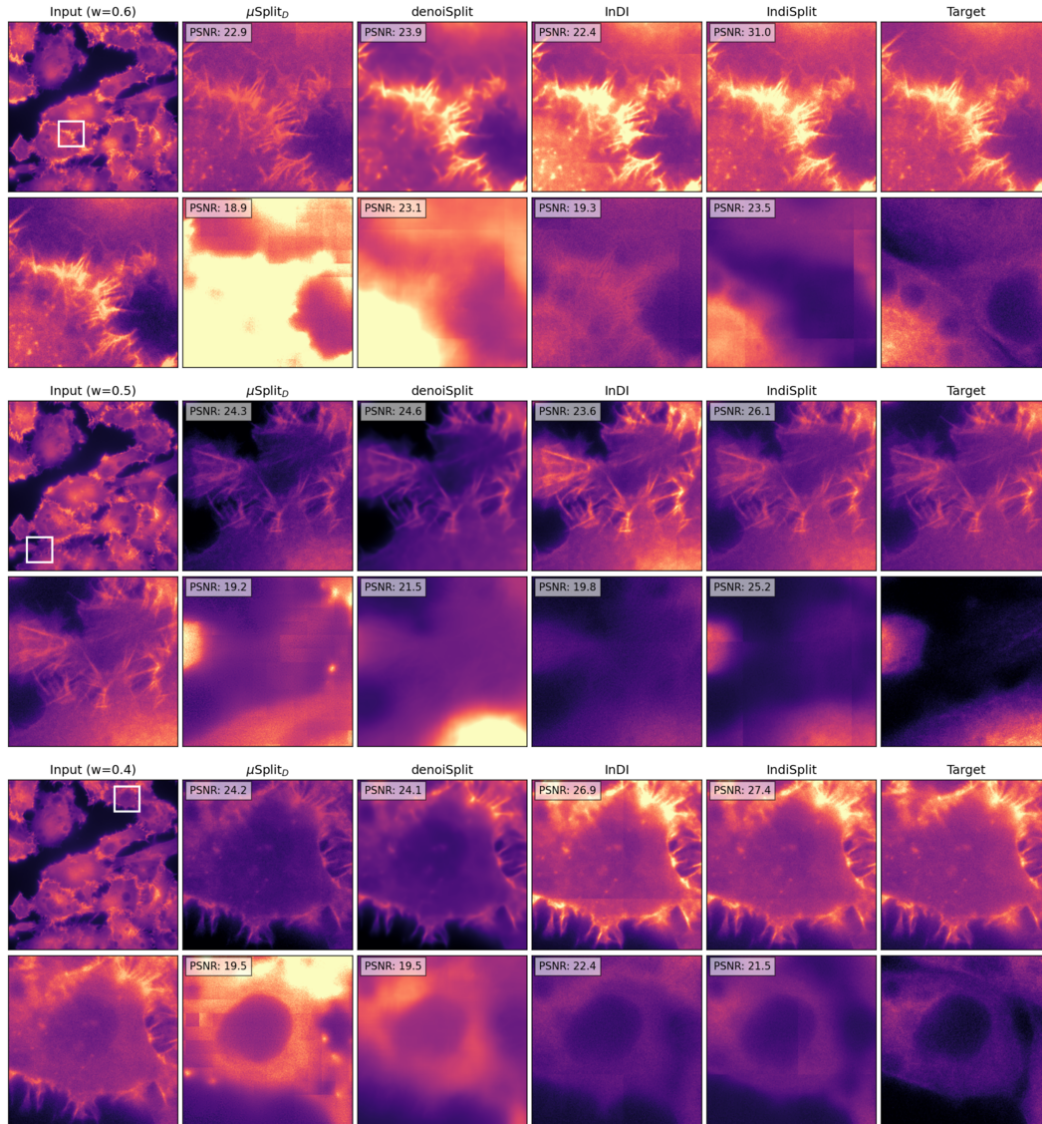


Figure S.16. Qualitative evaluation for PaviaATN dataset. In each panel, we show the full input frame (top-left) and the zoomed-in input patch (bottom-left) for which we show the predictions and the targets (last col) for the two channels, one in each row. We also report PSNR values for the patch shown. The w value reported on top of the input column is for the first channel. It naturally becomes $1 - w$ for the second channel.

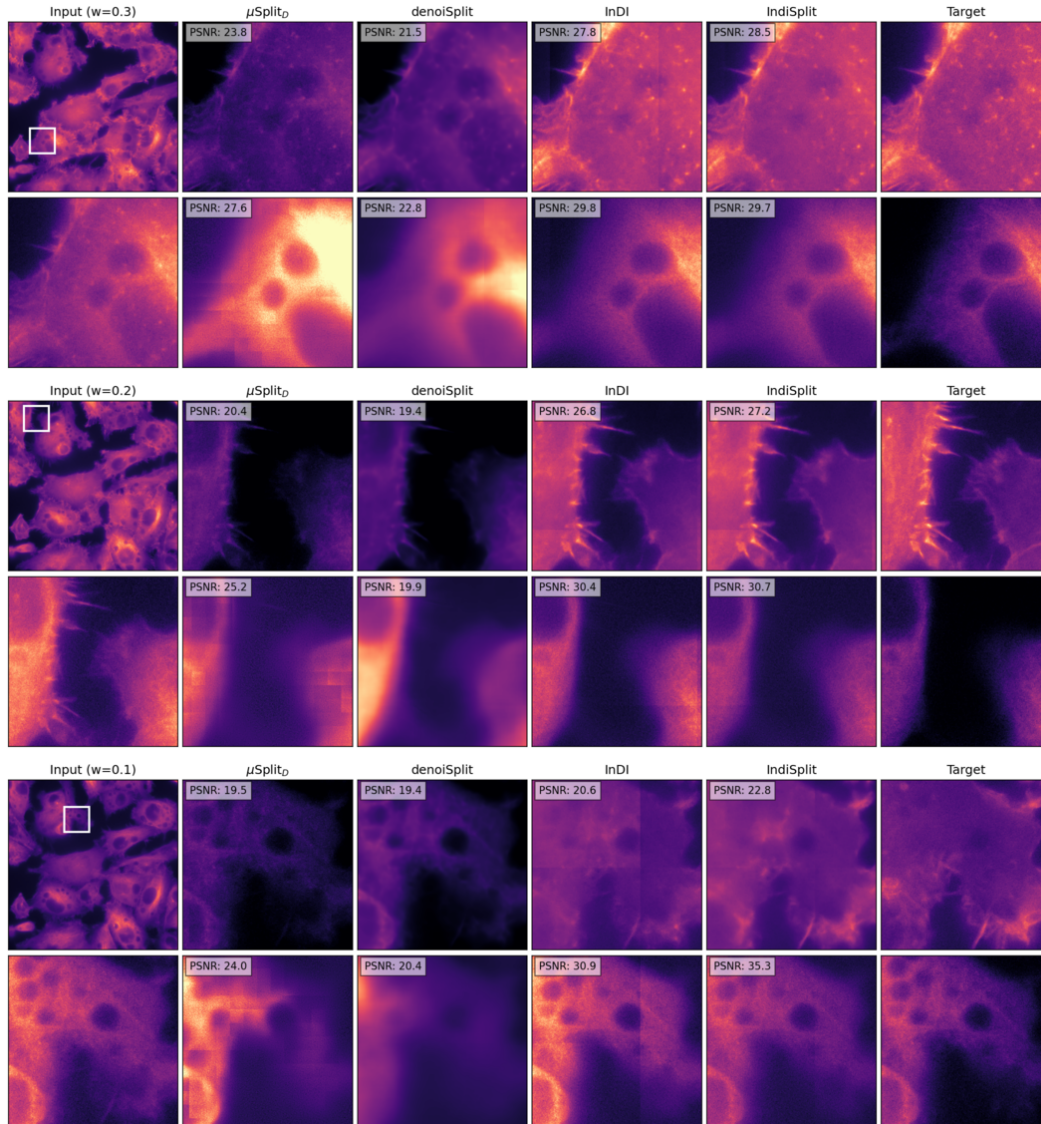


Figure S.17. Qualitative evaluation for PaviaATN dataset. In each panel, we show the full input frame (top-left) and the zoomed-in input patch (bottom-left) for which we show the predictions and the targets (last col) for the two channels, one in each row. We also report PSNR values for the patch shown. The w value reported on top of the input column is for the first channel. It naturally becomes $1 - w$ for the second channel.

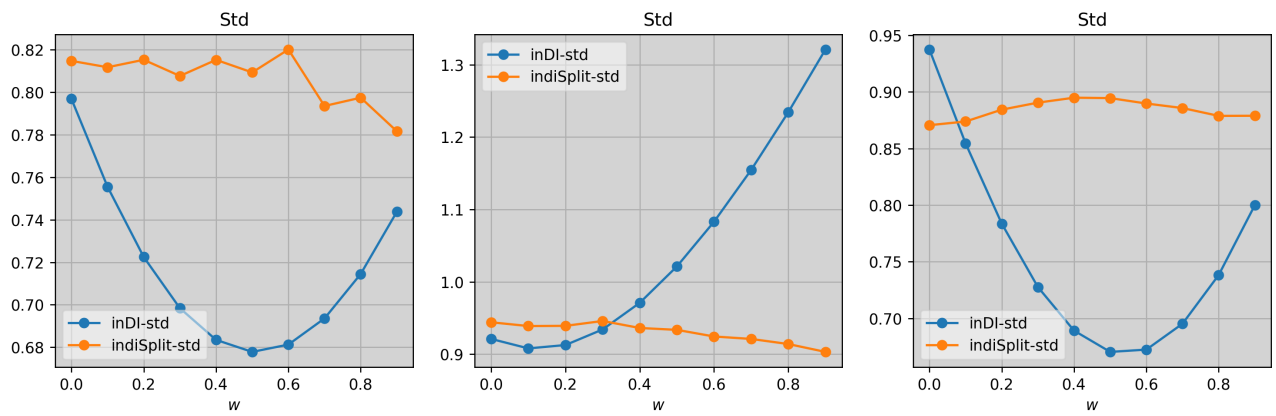


Figure S.18. Analysis of input patch variability across mixing factors w using 2000 randomly sampled 512×512 image pairs (c_0, c_1) : (a) Supervised image restoration models like InDI [12] normalizes c_0 and c_1 separately before interpolation, resulting in input patches with standard deviation strongly correlated with w ; (b) our proposed method decouples this relationship. Results across Hagen et al. (left), HTLIF24 (center), and BioSR (right) datasets demonstrate reduced dependency on w with our approach.